

## **TNO INTERNAL**

Westerduinweg 3 1755 LE Petten P.O. Box 15 1755 ZG Petten

The Netherlands

TNO report

www.tno.nl

TNO 2020 R10931 APPWRAP Project

T +31 88 866 50 65

Date June 2020

Author(s) H. Özdemir, A. K. Ravishankara, I. Bakhmet, M. Caboni

Copy no No. of copies

Number of pages 66 (incl. appendices)

Number of appendices 5

Sponsor Topsector Energy Subsidy from the Dutch Ministry of Economic Affairs and Climate

Project name Aerodynamics Performance Enhancement by Leading Edge Protective Wraps "APPWRAP"

Project number 060.38598

#### All rights reserved.

No part of this publication may be reproduced and/or published by print, photoprint, microfilm or any other means without the previous written consent of TNO.

In case this report was drafted on instructions, the rights and obligations of contracting parties are subject to either the General Terms and Conditions for commissions to TNO, or the relevant agreement concluded between the contracting parties. Submitting the report for inspection to parties who have a direct interest is permitted.

© 2020 TNO

## Summary

Innovations in leading edge protective wraps or protective coatings are currently being developed to counter the effects of leading edge erosion and damage on wind turbine blades. Concurrently, the design and development of vortex generators (VGs) is taking place to counter aerodynamic stall and enhance the aerodynamic performance of wind turbine blades. This project aims at research and analysis for the refinement of the design and development of an innovative solution, namely "fit-for-purpose sleeve", which can couple the leading edge protection with the vortex generators (VGs) and analyze the performance of these VGs with a CFD method developed within this project.

One of the main tasks of this project is to first complete the development of a pressure-based incompressible Navier-Stokes method and implement it in the open source CFD suite SU2, for wind energy applications and then apply it for the above mentioned VG design and finally analyze the effect on the performance on a blade. As the first main deliverable the development of the CFD method is completed and the method together with verification and validation is published on various platforms including the AIAA SciTech 2020 Conference.

In the second part of the project the main goal was to apply this new pressure-based method to simulate airfoil sections with and without VGs. For this purpose the generic AVATAR blade is chosen as the base blade and Laminar Flow Technology Limited (LFTL) has performed the VG design.

First, the CFD simulations were carried out on the five "clean" airfoil sections (without VGs) of the AVATAR blade and lift and drag polars as well as pressure coefficient distributions are obtained. It is shown that these CFD simulation results are in good agreement with the numerical results obtained by the in-house aerodynamic design and analysis tool RFOIL.

After the final VG configuration details were received from LFTL, body fitted VG meshes were generated for DU346, DU396 and DU600 sections of the AVATAR blade. Initially, the simulations were performed for DU346 and DU396 airfoil sections for various Re numbers and angle of attacks. The analysis of these simulations revealed that the performance of the VGs did not match the expectations e.g. they decreased the lift and increased the drag considerably while an increase in lift and a slight increase in drag coefficients were expected.

Although the performance analysis of the blade with and without VGs was not completed, the newly developed CFD method can be applied to critical wind energy problems in the follow-up projects. Furthermore, within this project, much experience gained in mesh generation for complex geometries as well as on the design methodology of blade add-ons like vortex generators.

# Contents

|     | Summary   | 2  |
|-----|---|----|
|     | List of tables and figures  | 4  |
| 1   | Project Details   | 7  |
| 1.1 | Goal of the project   | 7  |
| 1.2 | Results   | 8  |
| 1.3 | Planning of the report and presented results                      | 10 |
| 2   | Development of pressure based incompressible Navier-Stokes method | 11 |
| 2.1 | Introduction  | 11 |
| 2.2 | Literature Study  | 11 |
| 2.3 | Model equations and numerical discretization                      | 13 |
| 2.4 | Verification  | 19 |
| 2.5 | Validation  | 20 |
| 3   | Vortex Generator design   | 26 |
| 3.1 | AVATAR blade  | 26 |
| 3.2 | Design iterations   | 27 |
| 4   | Mesh topology   | 31 |
| 4.1 | Airfoil sections without VG                                       | 31 |
| 4.2 | Airfoil sections with VG  | 32 |
| 5   | Simulation Results of Airfoil Sections for Clean and VG Cases     | 34 |
| 5.1 | Mesh refinement study   | 34 |
| 5.2 | Clean airfoil sections  | 34 |
| 5.3 | Simulation results  | 36 |
| 5.4 | Airfoil sections with a VG  | 45 |
| 6   | Conclusions   | 51 |
| 7   | References  | 53 |
| A   | VG design: co-rotating series 1 version 1                         | 57 |
| В   | VG design: co-rotating series 2 version 1                         | 59 |
| С   | VG design: counter-rotating series 1 version 1                    | 61 |
| D   | VG design: counter-rotating series 2 version 1                    | 63 |
| F   | VG design: counter-rotating series 2 version 1 - final dimensions | 65 |

# List of tables and figures

| 1        | Airfoil sections used for the AVATAR rotor.   | 26  |
|----------|---|-----|
| 2        | Blade description (based on the AVATAR rotor).  | 26  |
| 3        | Simulation matrix for the clean cases   | 35  |
| 4        | Simulation matrix for the clean cases   | 35  |
| 5        | Simulation matrix for the VG cases.   | 45  |
| Figu     | res   |     |
| 1        | Dual grid on 2-D square grid.   | 14  |
| 2        | Channel flow schematic (a) and velocity profile comparison between numerical and analytical solution at different grid resolutions.                   | 19  |
| 3        | Channel flow error norm (a) and convergence history (b).  | 19  |
| 3<br>4   | Couette flow  | 20  |
|          |   | 20  |
| 5        | Flat plate domain (a) and skin friction comparison between numerical and  | 24  |
| ^        | Basius solution (b)   | 21  |
| 6        | Comparison of $x$ — component of velocity to the Blasius solution for lami-   | 04  |
| _        | nar flow over a flatplate   | 21  |
| 7        | Comparison of $y$ —component of velocity to the Blasius solution for lami-  | ~ 4 |
| _        | nar flow over a flatplate   |     |
| 8        | Laminar flow over a cylinder at $Re = 40$ .   |     |
| 9        | Results from inviscid flow over NACA 0012.  | 22  |
| 10       | Laminar flow over a backward facing step. Comparison of velocity profiles obtained from the numerical results with the literature at two different x- |     |
|          | locations (a) and streamlines showing the two recirculating zones along   |     |
|          | the bottom and top walls (b)  | 23  |
| 11       | Comparison of the velocity profile obtained from pressure based (PB) and  |     |
|          | density based (DB) methods in SU2 and reference solution[1] along the   |     |
|          | centerline( $x = 0.5$ ) for lid driven cavity, $Re = 400$   | 24  |
| 12       | Turbulent flow over a flat plate at $Re = 5e6$  | 24  |
| 13       | Turbulent flow over NACA0012 airfoil. A comparison of the numerical   |     |
|          | solution with the experimental data for lift to drag ratio (left) and lift coef-  |     |
|          | ficient for various angle of attacks (right).   | 25  |
| 14       | Sketch of the VG configuration showing the locations on AVATAR blade  | 28  |
| 15       | Sketch of the VG configuration detail iteration 1.  | 28  |
| 16       | Sketch of the VG configuration detail iteration 1.  | 28  |
| 17       | Sketch of the VG configuration detail iteration 2.  | 29  |
| 18       | Final requested dimensions of the VG configuration detail iteration 2   | 29  |
| 19       | DU300 2d mesh of the airfoil (left) and zoomed into the BL (right)  | 31  |
| 20<br>21 | Details of the DU300 mesh. Boundary layer (left) and Trailing edge (right). A sketch of a counter-rotating VG orientation and placement on an ex-     | 31  |
|          | truded airfoil section (blue region). Top view  | 32  |

| 22 | (left)   | 33 |
|----|--|----|
| 23 | DU396 mesh topology around VG (right) and top view showing orientation   | 33 |
| 24 | (left).  DU600 mesh topology around VG (right) and top view showing orientation (left).  | 33 |
| 25 | Comparison of the pressure coefficient (left) and the skin friction coefficient (right) at an $AoA=2.5^\circ$ , $Re=2.0\times10^6$ for different grid resolutions. | 34 |
| 26 | Lift (left) and drag (right) polars for the fully turbulent(clean) case at $Re=2.0\times 10^6.$  | 35 |
| 27 | DU 97-W-240 airfoil profile.   | 37 |
| 28 | A comparison of lift (left) and drag (right) polar for DU240 for $Re=2.0 	imes 10^6$ obtained from Rfoil and SU2 numerical simulations                             | 37 |
| 29 | A comparison of lift (left) and drag (right) polar for DU240 for $Re=9.0 \times 10^6$ obtained from Rfoil and SU2 numerical simulations                            | 37 |
| 30 | A comparison of lift (left) and drag (right) polar for DU240 for $Re=16.0 \times 10^6$ obtained from Rfoil and SU2 numerical simulations                           | 37 |
| 31 | A comparison of pressure coefficients (Cp) for a Re number of $2.0 \times 10^6$ for $1.5^\circ$ (design angle of attack) and $10^\circ$ for DU240                  | 38 |
| 32 | A comparison of pressure coefficients (Cp) for the design Re number of $16.0 \times 10^6$ for $1.5^\circ$ (design angle of attack) and $10^\circ$ for DU240        | 38 |
| 33 | DU 97-W-300 airfoil profile.   | 38 |
| 34 | A comparison of lift (left) and drag (right) polar for DU300 for $Re=2.0 	imes 10^6$ obtained from Rfoil and SU2 numerical simulations                             | 38 |
| 35 | A comparison of lift (left) and drag (right) polar for DU300 for $Re=9.0 \times 10^6$ obtained from Rfoil and SU2 numerical simulations                            | 39 |
| 36 | A comparison of lift (left) and drag (right) polar for DU300 for $Re=16.0 \times 10^6$ obtained from Rfoil and SU2 numerical simulations                           | 39 |
| 37 | A comparison of pressure coefficients (Cp) for a Re number of $2.0 \times 10^6$ for $2.5^\circ$ (design angle of attack) and $10^\circ$ for DU300                  | 39 |
| 38 | A comparison of pressure coefficients (Cp) for the design Re number of $16.0 \times 10^6$ for $2.5^\circ$ (design angle of attack) and $10^\circ$ for DU300        | 39 |
| 39 | DU 97-W-346 airfoil profile.   | 40 |
| 40 | A comparison of lift (left) and drag (right) polar for DU346 for $Re=2.0 \times 10^6$ obtained from Rfoil and SU2 numerical simulations                            | 40 |
| 41 | A comparison of lift (left) and drag (right) polar for DU346 for $Re=8.0 \times 10^6$ obtained from Rfoil and SU2 numerical simulations                            | 40 |
| 42 | A comparison of lift (left) and drag (right) polar for DU346 for $Re=14.5 \times 10^6$ obtained from Rfoil and SU2 numerical simulations                           | 40 |
| 43 | A comparison of pressure coefficients (Cp) for a Re number of $2.0\times10^6$ for $3.5^\circ$ (design angle of attack) and $10^\circ$ for DU346                    | 41 |
| 44 | A comparison of pressure coefficients (Cp) for the design Re number of $14.5 \times 10^6$ for $3.5^\circ$ (design angle of attack) and $10^\circ$ for DU346        | 41 |
| 45 | DU 97-W-396 airfoil profile.   | 41 |
| 46 | A comparison of lift (left) and drag (right) polar for DU396 for $Re=2.0 	imes 10^6$ obtained from Rfeil and SU2 numerical simulations                             | 11 |

| 47  | A comparison of lift (left) and drag (right) polar for DU396 for $Re=2.0 \times 10^6$ obtained from Rfoil and SU2 numerical simulations | 42  |
|-----|---|-----|
| 48  | A comparison of lift (left) and drag (right) polar for DU396 for $Re=12.5 	imes$  |     |
| .0  | $10^6$ obtained from Rfoil and SU2 numerical simulations  | 42  |
| 49  | A comparison of pressure coefficients (Cp) for a Re number of $2.0 \times 10^6$   |     |
| . • | for $4.5^{\circ}$ (design angle of attack) and $10^{\circ}$ for DU396   | 42  |
| 50  | A comparison of pressure coefficients (Cp) for the design Re number of  |     |
|     | $12.5 \times 10^6$ for $4.5^\circ$ (design angle of attack) and $10^\circ$ for DU396  | 42  |
| 51  | DU 97-W-600 airfoil profile.  | 43  |
| 52  | A comparison of lift (left) and drag (right) polar for DU600 for $Re=2.0	imes$  |     |
|     | 10 <sup>6</sup> obtained from Rfoil and SU2 numerical simulations   | 43  |
| 53  | A comparison of lift (left) and drag (right) polar for DU600 for $Re=5.0 	imes$   | . • |
|     | $10^6$ obtained from Rfoil and SU2 numerical simulations  | 43  |
| 54  | A comparison of lift (left) and drag (right) polar for DU600 for $Re=8.5	imes$  | . • |
| •   | $10^6$ obtained from Rfoil and SU2 numerical simulations  | 43  |
| 55  | A comparison of pressure coefficients (Cp) for a Re number of $2.0 \times 10^6$   | . • |
|     | for $2^{\circ}$ and $8.0^{\circ}$ for DU600.  | 44  |
| 56  | A comparison of pressure coefficients (Cp) for the design Re number of  |     |
|     | $8.5 \times 10^6$ for $0^\circ$ and $10.5^\circ$ (design angle of attack) for DU600   | 44  |
| 57  | Planes along the span direction of the airfoil section where Cp curves are  |     |
|     | extracted.  | 45  |
| 58  | Lift (left) and drag (right) polar for DU346 with VG for $Re=13.0 \times 10^6$ and  |     |
|     | $Re = 14.5 \times 10^6$ compared with the clean case for a $Re = 14.5 \times 10^6$  | 46  |
| 59  | A comparison of pressure coefficients (Cp) for the clean and VG cases   |     |
|     | for DU346 airfoil section. $Re = 14.5 \times 10^6$ , $AoA = 3.5^\circ$  | 46  |
| 60  | Lift (left) and drag (right) polar for DU396 with VG for $Re=2.0 \times 10^6$   |     |
|     | compared with the clean case.   | 47  |
| 61  | A comparison of pressure coefficients (Cp) for the clean and VG cases   |     |
|     | for DU396 airfoil section. $Re = 2.0 \times 10^6$ , $AoA = 4.5^\circ$   | 47  |
| 62  | Lift (left) and drag (right) polar for DU396 with VG for $Re=12.5 	imes 10^6$   |     |
|     | compared with the clean case.   | 47  |
| 63  | A comparison of pressure coefficients (Cp) for the clean and VG cases   |     |
|     | for DU396 airfoil section. $Re=12.5\times10^6$ , $AoA=4.5^\circ$  | 48  |
| 64  | Vorticity magnitude for DU346 $Re=12.5\times10^6$ , $AoA=2.0^\circ$ (left) with   |     |
|     | contours (right)  | 48  |
| 65  | Vorticity on the planes behind the VG for DU346 $Re=12.5 \times 10^6$ , $AoA=$  |     |
|     | 2.0°  | 49  |
| 66  | Velocity behind the VG for DU346 $Re=12.5\times10^6$ , $AoA=2.0^\circ$ (left)   |     |
|     | $AoA = 12.0^{\circ}$ (right)  | 49  |
| 67  | Vorticity behind the VG for FFA241 $Re=1.6\times10^6$ , $AoA=8.8^\circ$ (an   |     |
|     | example simulation with a conventional VG design)   | 49  |
| 68  | Boundary layer profiles on the airfoil near the VG for DU 396 with S2V1   |     |
|     | with $h=0.121m$ for an airfoil section with a chord length of $\ 6.0m$ (left)   |     |
|     | and for a conventional VG with $h=0.005m$ for an airfoil section with a   |     |
|     | chord length of 1.0m (right).   | 50  |

## 1 Project Details

### 1.1 Goal of the project

#### **Background and Motivation**

A variety of atmospheric and environmental conditions can adversely affect the leading edge of wind turbine blades and reduce power generation. To diminish the effects of blade erosion, protective coatings or wraps are applied to the leading edge of the blade. This process can be done either pre- or post-production/construction of the blade, where typically post installation applications can be achieved with limited downtime of the turbine.

Furthermore, structural and aerodynamic loads cause the root chord of wind turbine blades to be of significant dimension and thus more prone to aerodynamic stall. The same stall effect is present in span as the relative airflow alters with differing environmental conditions. To counter this, blades can be equipped with vortex generators to produce vortices in the boundary layer, reduce flow separation at slower speeds and higher angles of attack. Additionally, the vortex generators increase lift at lower angles of attack, increasing efficiency of the turbine. These too, are typically applied either pre or post production/construction of the blade.

In the project, Laminar Flow Technology Limited develops an innovative solution that incorporates both leading edge protection and the improved aerodynamics that can be applied to currently operational wind turbines as well as new constructions. This innovative solution, namely "fit-for-purpose sleeve", will be manufactured out of the best material to provide optimal, light weight erosion benefits with substantial durability, and limit the negative effects of a small backward facing step along the blade in span. The vortex generator fits into apertures incorporated into the leading edge "sleeve" material, thus ensuring both orientation and geometry in chord and span. This allows for ease of application whilst providing custom stall benefits to the particular wind turbine blade.

The vortex generators are of a bespoke design, the geometry of which requires careful consideration. The vortex generator energizes the boundary layer by mixing high energy external flow with the boundary layer which allows for the boundary layer to remain attached for longer, delaying stall and increasing lift. The location and geometry of the vortex generator, thus, has a significant effect on the performance of the turbine blade.

The development of the "fit-for-purpose sleeve" requires accurate analysis of the effect of different vortex generator configurations. TNO is developing a CFD method which can be applied to analyze the performance of these vortex generators. The method will be implemented to an existing open source CFD suite SU2.

### **Contribution to TKI Offshore Wind Programme**

This project falls under the "cost reduction and optimisation" part of the TKI Wind op Zee programme. Important drivers for reducing wind farm cost of energy include increasing energy output, decreasing O&M costs and lifetime extension. A cheap and effective method for avoiding erosion and at the same time improving production will lead to significant cost reductions.

The development of a CFD-solver to calculate accurately the aerodynamics of large offshore wind turbine blades benefits many wind turbine developers and developers of innovations. The CFD-solver is being developed by a TNO-PhD and is an open-source code. That means that all improvements become available for everybody.

The collaboration on validation and practical applications makes the improvements of the CFD-code valuable: improvements of codes without proper validation have no value in a design process because the risks and accuracies are not known.

#### 1.2 Results

Laminar Flow Technology Limited and TNO Wind Energy will carry out a project to investigate Leading Edge Protection Design, Vortex Generator Design and Trailing Edge Tab Design with the specific objective of it being a "fit-for-purpose sleeve", as well as whether this innovative solution may be used for blade root spoilers. This project consists of 2 work packages:

## WP1 - Innovation research (IO):

- investigate the best possible materials and adhesives to be used for the sleeve (LFTL)
- optimizing prime orientation and dimension to suit a specific blade geometry (LFTL)
- quantifying performance enhancements (erosion protection; stall characteristics; acoustic signature reduction, etc.) (LFTL)
- evaluating mold design techniques and procedures as well as the modalities of manufacturing (LFTL)
- determining installation processes and maintenance requirements (LFTL)
- CFD (Computational Fluid Dynamic) modelling and real world data analysis of the interaction and interdependence of the VG's and root spoilers (LFTL, TNO Wind Energy)
- Development of numerical methods and approaches tailored for design and analysis of enhanced turbine blades (TNO Wind Energy) including the validation efforts and the development of practical use cases. A medior researcher will apply the developed code of the PhD to this case in order to prove that the code is functioning well and gives reliable answers.

#### WP2

- Developing an open source CFD solver into an incompressible CFD solver so that the effects of the innovation can be accurately determined (TNO Wind Energy)
- A PhD at TNO Wind Energy is working on the development of a CFD solution. An open source CFD solver is modified for the application of wind energy. The physics solutions that needs to be changed within this computer model is that the compressible solver needs to modified to a non-compressible solver. This means that shock waves (for airplanes) cannot be modelled. Because wind turbines operate in lower speeds than airplanes and at the same time have much larger blades, it is essential to modify the solver. Especially in the root region (near the hub of the rotor), the speeds are low and the compressible solver does not give accurate answers (or will fail completely).

## The project result in:

- quantifying the efficacy of the performance enhancements of the current design and highlighting areas that require further detailed research
- cross-validating the CFD analyses of Laminar Flow Technology Limited and TNO Wind Energy, design computations and assumptions
- enhancing the selection of materials and adhesives, thereby augmenting the modalities of the molded technology
- optimized individual VG's to a bespoke chord specification and span location to provide the highest degree of efficiency
- an incompressible solver implemented in SU2 CFD software with the capability to analyze vortex generators and blade erosion

The results of the calculations, computations, assumptions and innovations as well as a description of the required infrastructure be reported in depth.

The project activities are as follows:

- Complete the development of incompressible (non-compressible) open source CFD solver.
- CFD modelling and simulations of VGs with a body fitted mesh.
- CFD modelling of root spoilers and analysis of the interaction with VGs.
- Perform analysis for the optimum VG configuration (location, geometry, etc.).
- Design a wrap for a large wind turbine blade. Blade input TNO Wind Energy, Calculations Laminar Flow Technology,

- Compare the CFD solutions with the data provided by Laminar Flow Technology for the validation of the results.
  - (a) Analyse the performance of VGs.
  - (b) Analyse the interaction of VGs with root spoilers.
  - (c) Analyse the overall performance improvement of the enhanced blade with VGs, root spoiler and leading edge "sleeve".

## 1.3 Planning of the report and presented results

In the remaining of this report the studies and the results concerning the above mentioned deliverables are presented.

In chapter 2 the main activities of the PhD student is presented that falls within the duration of this project. The details of the developed pressure based incompressible Navier-Stokes method is shown together with the verification and validation cases. The contents of this chapter are from the recently published article at the SciTech 2020 conference[2, 54]. Further, a model to quantify the effect of leading edge erosion was also implemented in the open source tool. A publication based on this model is under peer review.

In chapter 3 the details of the vortex generator design by LFTL is presented. Also, the choice of the airfoil sections for the numerical simulations together with the generic AVATAR blade details are given in this chapter.

Chapter 4 mainly describes the mesh topology for the 2D clean airfoil sections and 3D airfoil sections including vortex generator.

In the results chapter (5) initially the simulation matrix is presented together with a mesh refinement study before presenting the results for the clean and VG simulation cases.

Finally in chapter 6 a detailed explanation on the simulation results for the VG cases is given. Some remarks and comments are presented to improve the current design.

## 2 Development of pressure based incompressible Navier-Stokes method

#### 2.1 Introduction

This chapter presents the details of the developed pressure based incompressible Navier-Stokes method which is the main goal of the "WP2 - Fundamental research". This chapter is already published at AIAA SciTech 2020 Forum[2] and repeated (and extended) here for the sake of completeness of the report.

## 2.2 Literature Study

Flows around wind turbines generally fall under the high Reynolds number and low Mach number regime that is somewhat unique and greatly advantageous in terms of numerical analysis. The high Reynolds number means large regions of the flow can be considered inviscid except for a small region around the body known as the boundary layer. The low Mach numbers imply that the flow remains incompressible. This combination of conditions have been exploited to develop a wide variety of numerical tools based on simplifications of the Navier-Stokes equations. Blade element momentum theory, based on global momentum balance across the wind turbine[3], has been extremely useful in determining wind turbine behavior and has been extended using empirical corrections[4] to account for more complicated effects. Other numerical methods based on inviscid theory like panel methods and lifting line theory[5] have been successfully used to compute flow around a wind turbine blade including the wake. Viscous inviscid interaction tools like RFOIL[6, 7] can be used in combination with the lifting line methods to account for the presence of a boundary layer on turbine blades. However as the size of the turbine blades has increased, issues like thick airfoils and transition modeling are becoming more important. Additionally, new concepts to improve the efficiency of the turbines (e.g. vortex generators) are becoming more common. While it is possible to extend the existing tools like RFOIL to account for some of the new problems[8, 9, 10] arising out of modern wind turbine blades, they are still limited in their scope of applicability. Thus, a higher fidelity general purpose tool like CFD becomes necessary. This, among other factors, motivated the development of a new open-source CFD method for the wind energy community. While other tools exist (e.g. OpenFOAM [11] (also open source), EllipSys2D/3D[12, 13]), we hope to leverage the excellent multi-physics capabilities of SU2[14, 15] and make it available for the wider wind energy community. Apart from wind turbine blade analysis, CFD methods has been extensively used for wind farm analysis[16] as well.

A pressure based incompressible RANS solver implemented within the open source multiphysics suite SU2[15, 14] is developed in this project. The equations are discretized on collocated unstructured grids using a second order finite volume method. The integration in time is carried out using Euler implicit and explicit methods. Two turbulence models, Spalart-Allamaras (SA)[17] and the Menter Shear Stress Transport (SST)[18], are available for turbulence modeling. Currently, the SA turbulence

model has been extended to treat natural transition by the Bas-Cakmakcioglu (BC) transition model[19] and the Langtry-Menter[20] transition model will be incorporated as the next step.

The main challenge in solving the incompressible flow equations lies in resolving the pressure-velocity coupling[21, 22, 23, 24, 25]. Physically this challenge arises due to the pressure disturbances travelling at the speed of sound which, under the incompressible flow assumption, is infinitely fast and leads to numerical problems. For compressible flow problems (with a finite speed of sound), the continuity equation acts as an evolution equation for density which can be used in conjunction with the energy equation and a gas law to obtain the pressure field. However as the continuity equation reduces to a divergence condition on the mass flux for incompressible flows and the energy equation is decoupled, there is no direct way to compute the pressure field. To alleviate this, the pressure can be eliminated from the equations using derived quantities like stream function and vorticity[26] which can then be solved to obtain the flow field. Such methods, however, do not generalize well into 3-D and the use of primitive variables (pressure and velocity) is preferred. The pressure-velocity coupling can be overcome using primitive variables in a variety of ways which are broadly classified as either "pressure-based" or "density-based" methods. An example of the density based method is the pseudo compressibility approach[27, 21, 28] where an artificial speed of sound is introduced in the continuity equation to mimic the compressible flow formulation. This method belongs to the more general approach of pre-conditioned compressible flow solution methods[29]. The existing incompressible solver in SU2 follows this approach and has been extended to variable-density flows and heat transfer applications[29]. Alternatively in a pressure based method the continuity equation is satisfied directly[22]. The combination of the continuity equations and the momentum equations can be used to obtain a condition for pressure which can then be used to solve the continuity and momentum equations. The earliest such approach is the marker-and-cell (MAC) method[30] where pressure is used as a mapping parameter to satisfy the continuity equation and a Poisson equation is solved for pressure. However, this method was expensive due to its iterative nature and requirement of a Poisson solution in every iteration. This was improved upon by solving for pressure and velocity corrections instead of full pressure equation leading to faster convergence. The semi-implicit pressure linked equations (SIMPLE) and SIMPLE-like algorithms[31, 32] are very popular for this type and is also implemented in the current paper.

Originally, these methods were developed for staggered grids, where pressure is stored at cell centers and velocities on the cell faces. This conserves the mass and also avoids the odd-even decoupling of pressure. Extension to collocated grids needs special attention. Momentum interpolation methods to compute the mass flux based on the formulation introduced by Rhie and Chow in [33] is adapted in the current paper to avoid the odd-even decoupling of pressure. Numerous authors[34, 35, 36, 37, 38] have pointed out the dependence of the original interpolation scheme on factors such as under-relaxation and time step size. Consequently, the original momentum interpolation scheme is adapted to account for such factors.

In the following sections, first the governing equations and the discretization schemes are described, followed by a section on verification and validation based on standard problems.

## 2.3 Model equations and numerical discretization

The general structure of the PDE solved in SU2 is of the form[15]

$$\partial_t U + \nabla \cdot \vec{F}^c - \nabla \cdot \vec{F}^v = Q \quad \text{in} \quad \Omega, \quad t > 0, \tag{2.1}$$

where U is the vector of state variables,  $\vec{F}^c$  are the convective flux,  $\vec{F}^v$  are the viscous flux and Q is a source term. In a pressure based approach, the momentum equations and the pressure correction equation are solved sequentially. The pressure correction equation is derived based on a combination of momentum and continuity equations. The following sections briefly outline the derivation.

## 2.3.1 Momentum equation

For the momentum equations, the terms in Eq. 2.1 are

$$U = \begin{bmatrix} u_1 \\ u_2 \\ u_3 \end{bmatrix}, \quad \vec{F}_i^c = \begin{bmatrix} \rho u_i u_1 \\ \rho u_i u_2 \\ \rho u_i u_3 \end{bmatrix}, \quad \vec{F}_i^v = \begin{bmatrix} \tau_{i1} \\ \tau_{i2} \\ \tau_{i3} \end{bmatrix}, \quad Q = -\vec{F}_i^p = \begin{bmatrix} \partial_1 P \\ \partial_2 P \\ \partial_3 P \end{bmatrix}$$
(2.2)

where  $\vec{v}=(u_1,u_2,u_3)$  is the velocity vector,  $\rho$  is the density, P is the static pressure and the viscous stresses are  $\tau_{ij}=\mu_{tot}\big(\partial_j v_i+\partial_i v_j-\frac{2}{3}\delta_{ij}\nabla\cdot\vec{v}\big)$ . The total viscosity coefficient,  $\mu_{tot}$  is the sum of the dynamic viscosity  $\mu_{dyn}$  and turbulent viscosity  $\mu_{tur}$ , which is computed via a turbulence model. The Spalart-Allmara(S-A) and the Mean Shear Stress Transport(SST) turbulence models can be used to compute  $\mu_{tur}$ .

## 2.3.1.1 Spatial discretization

The spatial discretization is performed on an edge based dual grid using a finite volume approach[24, 23, 39]. The control volumes are constructed using a median-dual (vertex-based) scheme[40, 15] (see Fig. 1). Integrating the Eq. 2.1 on the domain  $\Omega$ ,

$$\int_{\Omega} \frac{\partial U}{\partial t} d\Omega + \int_{\Omega} \nabla (\vec{F}^c - \vec{F}^v) d\Omega = -\int_{\Omega} \nabla P d\Omega, \tag{2.3}$$

$$\int_{\Omega} \frac{\partial U}{\partial t} d\Omega + \int_{\partial \Omega} (\tilde{F}^c - \tilde{F}^v) \cdot d\vec{S} = -\int_{\partial \Omega} P I \cdot d\vec{S}, \tag{2.4}$$

$$\int_{\Omega} \frac{\partial U}{\partial t} d\Omega + R(U) = -F^p, \tag{2.4}$$

where  $F^p = |\Omega| \nabla P$  is the pressure contribution treated as a source term and R(U) is the residual vector consisting of the discretized convective and viscous fluxes,  $\tilde{F}^c$  and  $\tilde{F}^v$ .

The convective fluxes are discretized using a standard upwind scheme and second order accuracy is achieved via reconstruction of variables on the cell faces by a MUSCL

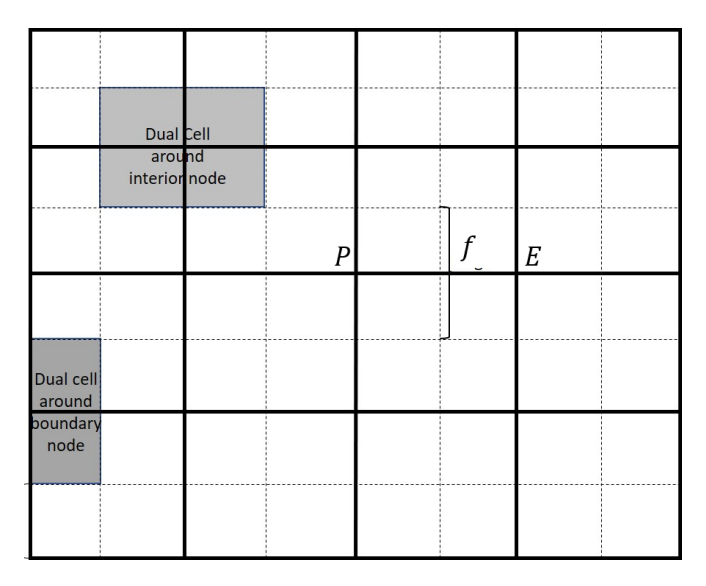


Figure 1: Dual grid on 2-D square grid.

scheme. The viscous discretization requires the evaluation of the gradients at the faces of control volumes. For a general variable  $\phi$  this gradient is evaluated as

$$\nabla \phi \cdot \vec{n} = \frac{\phi_j - \phi_i}{|x_j - x_i|} \alpha_f + \frac{1}{2} (\nabla \phi|_i + \nabla \phi|_j) \cdot (\vec{n} - \alpha_f \vec{s}), \tag{2.5}$$

where  $\vec{n}$  is the face normal,  $\vec{s}$  is the normalised vector connecting the cell centers i and j across the face,  $|x_j-x_i|$  is the distance between the nodes i and j and  $\alpha_f=\vec{s}\cdot\vec{n}$ . The gradients at cell centers i and j can be computed using either the Green-Gauss or the least squares theorem.

## 2.3.1.2 Time integration

Steady state solutions are found using a psuedo time step approach where a local time step acts as the under relaxation parameter. The steady state solution is found by integrating the governing equations for a long time. Following the approach outlined in [15] the solution update  $\Delta U_i^n = U_i^{n+1} - U_i^n$  of an element i for implicit time stepping is

$$\left(\frac{|\Omega|}{\Delta t_i^n} \delta_{ij} + \frac{\partial R_i(U^n)}{\partial U_j}\right) \Delta U_j = -R(U^n) - F_i^p, \tag{2.6}$$

where n indicates the current time level. A local time stepping scheme is used to accelerate the convergence as each cell advances at a suitable local time step.

## 2.3.2 Continuity equation

The continuity equation in the discrete form is

$$\sum_{f} \dot{m}_f = \sum_{f} \rho \vec{U}_f \cdot \vec{n}_f = 0, \tag{2.7}$$

where  $\vec{U}_f$  is the velocity at a face f,  $\rho$  is the fluid density and  $\vec{n}_f$  is the face normal. Using a linear interpolation to find this face velocity leads to the checkerboard problem in pressure and thus momentum interpolation techniques are used. This can also be interpreted as adding a third order derivative of pressure to stabilize the oscillations in the pressure field.

## 2.3.2.1 Momentum interpolation of velocities

Consider a face f between two nodes P and E (Fig. 1). Denoting the matrix  $\left(\frac{|\Omega|}{\Delta t}\delta_{ij} + \frac{|\Omega|}{\Delta t}\delta_{ij}\right)$ 

$$\left( rac{\partial R_i}{\partial U_j} 
ight)$$
 in Eq. 2.6 by the matrix  $oldsymbol{A}_{ij}$  , we have

$$\mathbf{A}_{ij}\Delta U_j = -R(U_i^n) - F_i^p,$$

which can also be written as

$$diag(\mathbf{A}_{ij})\Delta U_j + \mathbf{N}_{ij}\Delta U_j = -R(U_i^n) - F_i^p,$$

where  $N_{ij}$  consists of the off-diagonal terms of the jacobian matrix  $A_{ij}$ . Thus, the velocity at any two points P and E at time level n+1 can be written as

$$U_{P} = U_{P}^{n} + \Delta U_{P} = U_{P}^{n} - \frac{1}{diag(\mathbf{A})} {}_{P} \Big( R(U^{n}) + \mathbf{N}_{P} \Delta U_{\mathcal{N}(P)} + F_{P}^{p} \Big), \tag{2.8}$$

$$U_{E} = U_{E}^{n} + \Delta U_{E} = U_{E}^{n} - \frac{1}{diag(\mathbf{A})} \left( R(U^{n}) + \mathbf{N}_{E} \Delta U_{\mathcal{N}(E)} + F_{E}^{p} \right).$$
 (2.9)

Here  $\mathcal{N}(P)$  represents the neighbors of any node P. We can hypothetically write the new velocity at a face f between P and E,  $U_f$  as,

$$U_f = U_f^n + \Delta U_f = U_f^n - \frac{1}{diag(\mathbf{A})} \left( R(U^n) + \mathbf{N}_f \Delta U_{\mathcal{N}(f)} + F_f^p \right). \tag{2.10}$$

Denoting  $B_P = diag(\mathbf{A})_P^{-1} \Big( R(U_P^n) + \mathbf{N} \Delta U_{\mathcal{N}(P)} \Big)$ , we can write

$$B_f = (\lambda_P B_P + \lambda_E B_E), \tag{2.11}$$

where  $\lambda_P$  and  $\lambda_E$  are the weighting factors for the interpolation. Using Eqs. 2.8, 2.9, 2.10 and 2.11 and expanding the pressure source term  $F^P$  from Eq. 2.4, the velocity at a face f after the momentum equation is

$$U_f^* = \left(\lambda_P U_P^* + \lambda_P U_E^*\right) - \frac{|\Omega|_f}{diag(\mathbf{A})_f} \nabla P_f + \left(\lambda_P \frac{|\Omega|_P}{diag(\mathbf{A})_P} \nabla P_P + \lambda_E \frac{|\Omega|_E}{diag(\mathbf{A})_E} \nabla P_E\right). \tag{2.12}$$

First, we assume

$$\left(\lambda_{P} \frac{|\Omega|_{P}}{diag(\mathbf{A})_{P}} \nabla P_{P} + \lambda_{E} \frac{|\Omega|_{E}}{diag(\mathbf{A})_{E}} \nabla P_{E}\right) = \frac{\overline{|\Omega|}}{diag(\mathbf{A})} \overline{\nabla P_{f}}$$
(2.13)

and let

$$\frac{|\Omega|_f}{diag(\mathbf{A})_f} = \frac{|\Omega|}{diag(\mathbf{A})},$$
$$\overline{U}_f = (\lambda_P U_P + \lambda_E U_E).$$

The estimated face velocity can now be written as

$$U_f^* = \overline{U_f^*} - \frac{\overline{|\Omega|}}{diag(\mathbf{A})} \Big( \nabla P_f - \overline{\nabla} \overline{P_f} \Big). \tag{2.14}$$

Since the solution from momentum equations do not yet satisfy the continuity constraint the velocities are denoted by  $U^*$ . The assumption made in Eq. 2.13 can be shown to be second order accurate[24]. The derivations so far follow the procedure outlined by Rhie-Chow[33] and no corrections[34, 35, 41, 36, 37, 38] have been applied to account for under-relaxation and time stepping.

## 2.3.2.2 Pressure Correction equation

Let the velocity corrections be defined as U', pressure corrections as P'. Similar to the velocity estimate at a face, the velocity correction relation based on pressure corrections can be written as,

$$U_f' = \overline{U_f'} - \frac{|\Omega|}{diag(\mathbf{A})} \left( \nabla P_f' - \overline{\nabla P_f'} \right). \tag{2.15}$$

Rewriting Eq. 2.7 in terms of estimated velocity and velocity corrections,

$$\sum_{f} \dot{m}_{f} = \sum_{f} (\dot{m}_{f}^{*} + \dot{m}_{f}') = 0, \tag{2.16}$$

where  $\dot{m}_f^*$  and  $\dot{m}_f'$  are the estimate and correction of the mass flux respectively.

From Eqs. 2.14, 2.15 and 2.7,

$$\sum_{f} \rho \left( \overline{U'_f} - \frac{|\Omega|}{diag(\mathbf{A})} \left( \nabla P'_f - \overline{\nabla P'_f} \right) \right) \cdot \vec{n}_f = -\sum_{f} \dot{m}_f^*, \tag{2.17}$$

$$-\sum_{f} \rho \overline{\frac{|\Omega|}{diag(\boldsymbol{A})}} \Big( \nabla P_f' \Big) \cdot \vec{n}_f = -\sum_{f} \dot{m}_f^* - \sum_{f} \rho \overline{U_f'} \cdot \vec{n}_f - \sum_{f} \rho \overline{\frac{|\Omega|}{diag(\boldsymbol{A})}} \overline{\nabla P_f'} \cdot \vec{n}_f.$$
 (2.18)

The terms under the overbar on the RHS depend directly on the neighbors and are neglected (this is the SIMPLE assumption). Thus, we have an equation for the pressure correction as,

$$-\sum_{f} \rho \frac{|\Omega|}{diag(\mathbf{A})} \left( \nabla P_f' \right) \cdot \vec{n}_f = -\sum_{f} \dot{m}_f^*. \tag{2.19}$$

The term  $\sum_f \dot{m}_f^*$  is calculated using the estimated velocities  $U_f^*$  in Eq. 2.14 and is treated as a source term. Eq 2.19 is a Poisson equation for the pressure correction which has to be solved sequentially with the momentum equations. Let  $\frac{|\Omega|}{diag(\mathbf{A})} \cdot \vec{n}_f = \overline{\mathbf{D}}_f$ , the pressure correction gradient in Eq. 2.19 is decomposed into an orthogonal (implicit,  $\overline{\mathbf{E}}_f$ ) and non-orthogonal (explicit,  $\overline{\mathbf{E}}_f$ ) contribution as

$$\nabla P_f' \cdot \overline{\mathbf{D}}_f = \nabla P_f' \cdot \overline{\mathbf{E}}_f + \nabla P_f' \cdot \overline{\mathbf{T}}_f \tag{2.20}$$

An over-relaxed approach is followed to discretize the implicit part of the pressure correction gradient. No under-relaxation is used for the Poisson solver. A multigrid method can be applied specifically for the Poisson problem to speed up the convergence, especially for unsteady problems.

#### 2.3.2.3 Pressure and velocity corrections

Finally, based on the solution to the pressure correction and the pressure correction field, the pressure and velocities at a node P can be corrected as

$$P_P^{n+1} = P_P^* + \alpha_p P', (2.21)$$

$$U_P^{n+1} = U_P^* + D_P \nabla P_P'. (2.22)$$

Here,  $D_P = \frac{|\Omega|}{diag(\mathbf{A})}$  is the ratio of the volume of the element to the momentum equation coefficients at the node P and  $\alpha_p$  is the under-relaxation factor which is explained in more detail in the following section. Typically, the velocity correction is also under-relaxed but instead here the pseudo time-stepping scheme is used.

## 2.3.3 SIMPLE family of algorithms

There are many popular schemes for the pressure-based methods and one of the more widely used algorithm is the SIMPLE[32] and its derivatives[24, 42, 43, 44]. In this paper, the SIMPLE, SIMPLEC and PISO algorithms are used.

#### 2.3.3.1 SIMPLE/SIMPLEC

In summary, to find the solution at time n+1 the following algorithm is employed:

- 1. Set the solution at n as the initial guess.
- 2. Solve the momentum equations Eq. 2.6 to find the estimated velocity  $U^*$ .
- 3. Find the mass flux at the faces  $m_f^*$  using the velocities from Eq. 2.14.
- 4. Assemble the pressure correction equation based on the mass fluxes and the momentum equation.
- 5. Solve the pressure correction equation (Eq. 2.19) to find the pressure and velocity corrections based on Eqs. 2.22 and 2.21.
- 6. The updated solutions are set as the solution at time n+1 and solve other scalar equations, like turbulence.

One of the key assumptions involved in deriving the pressure correction equation was neglecting the terms involving the pressure and velocity corrections of neighbors. While this does not affect the final solution as all corrections go to zero at convergence, it does slow down the rate of convergence. Many improvements are employed to improve the speed of convergence.

One such improvement is to modify the under-relaxation used during the pressure correction in Eq. 2.21. The underrelaxation factor for pressure,  $\alpha_P$  is set as  $1-\alpha_U$ , where  $\alpha_U$  is the velocity under-relaxation. While there is no explicit under-relaxation applied to the velocity equation, the pseudo time step acts like an under-relaxation. Thus, the pressure under-relaxation is

$$\alpha_P = \frac{(|\Omega|/\Delta t)_{P,U}}{1 + (|\Omega|/\Delta t)_{P,U}}.$$
(2.23)

Another variation that is implemented in the current work is the SIMPLEC algorithm. The velocity correction at any node P is assumed to be the weighted average of the corrections at the neighboring points. This leads to a smaller term being neglected from the pressure correction, thus improving the speed of convergence. There is only a modification of the coefficients of the pressure correction equation compared to the SIMPLE algorithm and the sequence of operations remains the same.

#### 2.3.3.2 PISO

In this variation, an additional correction step is employed. The same sequence of operations outlined for SIMPLE is followed, and the corrected velocity and pressure

field is used to explicitly solve the momentum equations to find a new estimate of the velocity field. Based on the explicit velocity solution, the mass imbalance is computed once again and the pressure correction is solved to find a newer estimate of velocity. The explicit solution recovers a portion of the neglected terms and aids in increasing the rate of convergence.

## 2.3.4 Boundary conditions

The boundary conditions available are Euler (flow tangency), no slip wall, velocity inlet, pressure outlet and symmetry boundaries. Eq. 2.6 is discretized using the median-dual or vertex-centered approach which is different from the conventional approaches[24, 45, 39, 46]. The node for the boundary control volume lies on the boundary face itself and thus special attention is required during application of boundary conditions[39]. Additionally, there is no need for momentum interpolation of velocities to compute mass flux across the face as the velocity on the boundary face is available from the solution.

The application of each of these boundaries for the momentum equations, mass flux computation and pressure correction equation is described below.

#### 2.3.4.1 Momentum equations

- Euler or flow tangency condition: This boundary condition specifies a zero normal flux across the boundary (e.g. inviscid wall). For the momentum equations, this is applied as a Neumann boundary with zero flux across the face. Mass flux across the face is also set to zero.
- 2. Wall (no-slip): This is a strong boundary condition and is generally used to impose a no slip condition on walls. Since the discretization is vertex-based the boundary node lies on boundary face and thus the velocity boundary condition can be enforced as a Dirichlet boundary condition. Mass flux across the face is also set to zero.
- 3. Inlet: For a prescribed velocity at the inlet, the velocity is imposed as a Dirichlet boundary condition similar to the wall boundary. However, the mass flux is not zero but can be easily computed based on the specified velocity.
- 4. Outlet: For a specified pressure outlet, a Neumann boundary condition is applied at the outlet. Similarly, the mass flux across the face is also computed using the latest estimate of the velocity.
- 5. Symmetry: A symmetry boundary does not only imply a zero flux across the face but also a reflection of the solution state across the boundary face. Consequently, a reflected state of the current state is computed and a Neumann boundary condition is applied. Massflux across the face is set to zero.
- 6. Farfield: Farfield boundaries are generally used in external flow simulations to denote the freestream conditions. This is treated as an inlet-outlet type boundary where a Dirichlet condition is used for incoming flow and a Neumann boundary for outgoing flow based on the nature of the flux at the boundary face.

7. Periodic: The control volumes around the periodic boundary nodes are initially treated as an internal node to compute the residual contributions from the respective neighbors and then the fluxes from the 'donor' face is added to the 'reciever' face eventually treating the two nodes as one control volume.

## 2.3.4.2 Pressure correction equations

If the pressure at a particular boundary is unknown (Euler wall, Wall, Inlet, Symmetry) it is treated as a Neumann boundary and the value of the pressure is updated based on the pressure correction. However, if the value of pressure is specified (Outlet with a specified pressure), the value of the pressure is fixed and the pressure correction is set to zero as a Dirichlet boundary condition.

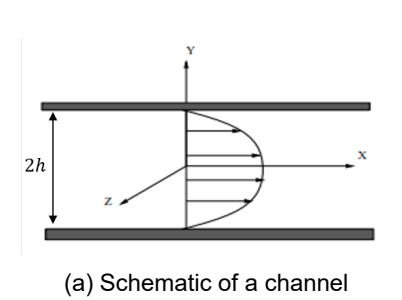
#### 2.4 Verification

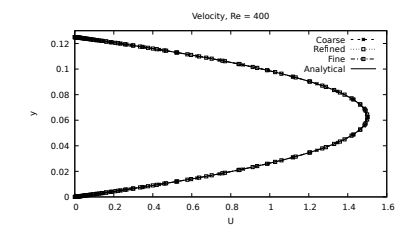
## 2.4.1 Laminar flow: Channel flow with analytical solution

To verify the order of accuracy of the solver, a fully developed laminar channel flow (schematic in Fig. 2a) with Re=400 is chosen. Under the fully developed flow assumptions, the velocity profile at any location y can be computed as

$$u(y) = -\frac{dP}{dx}\frac{1}{2\mu}(h^2 - y^2),$$
(2.24)

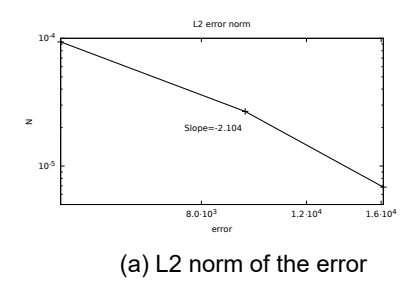
where  $\frac{dP}{dx}$  is the pressure gradient across the channel,  $\mu$  is the laminar viscosity, h is the half channel width.

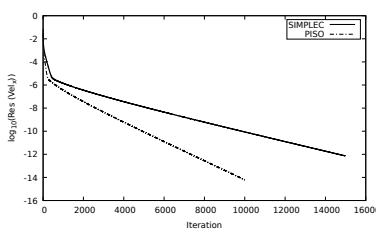




(b) Comparison of numerical and analytical results.

Figure 2: Channel flow schematic (a) and velocity profile comparison between numerical and analytical solution at different grid resolutions.





(b) Convergence history.

Figure 3: Channel flow error norm (a) and convergence history (b).

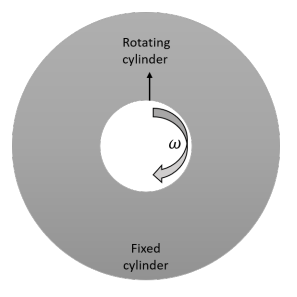
Three different mesh resolutions are chosen and the numerical results are compared to the analytical solution (Fig. 2b). The error in the numerical solution is computed for

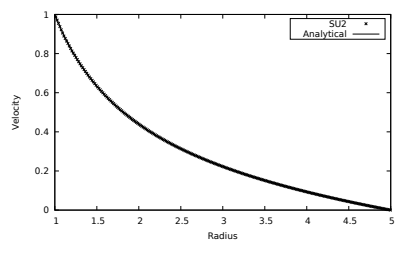
the three meshes and the order of accuracy can be seen to be second order (Fig. 3a), as expected. Convergence history is also shown for the coarse grid with SIMPLEC and PISO algorithms (Fig. 3b). As expected, the PISO algorithm converges to the final solution faster than the SIMPLEC algorithm.

#### 2.4.2 Couette flow

Couette flow can be described as the laminar flow between two concentric rotating cylinders. The schematic for Couette flow is shown in Fig. 4a with  $r_0$  as the inner radius and  $r_1$  as the outer radius.  $\omega_1$  and  $\omega_2$  refer to the angular velocities of the two cylinders. The analytical solution for the velocity as a function of radius r can be described as

$$u_{\theta}(r) = r_0 \omega_0 \frac{r_1/r - r/r_1}{r_1/r_0 - r_0/r_1} + r_1 \omega_1 \frac{r/r_0 - r_0/r}{r_1/r_0 - r_0/r_1},$$
(2.25)





- (a) Schematic of Couette flow.
- (b) Comparison of numerical and analytical results.

Figure 4: Couette flow.

The simulation was carried out on a domain with  $r_0=1$  and  $r_1=5$  units. The outer wall is held fixed and the inner wall is rotating at an angular velocity  $\omega_0=1$  rad/s. Fig. 4b shows the comparison of velocity along y=0. We observe a very good agreement between the numerical and analytical solution

#### 2.5 Validation

#### 2.5.1 Laminar flow over a flat plate

The results from the laminar flow over a flat plate (Re=4e5) is compared to the Blasius solution [47] at different locations (Figs. 6a 6b, 7a, 7b). The domain and the mesh used for the simulation is shown in Fig. 5a. A uniform inflow is prescribed and a small inflow region with a symmetry boundary is used before the flat plate begins. Nodes are clustered at near the wall and stretched away from it in the normal direction and clustered around the interface between the symmetry and the wall region and stretched towards the outlet in the streamwise direction.

The results for the streamwise component (Figs. 6a and 6b) of the velocity shows excellent agreement between the numerical and Blasius solution for both the density-based and pressure-based methods. The comparison for the normal velocity component (Figs. 7a and 7b) is not as good but it can be seen that the pressure-based

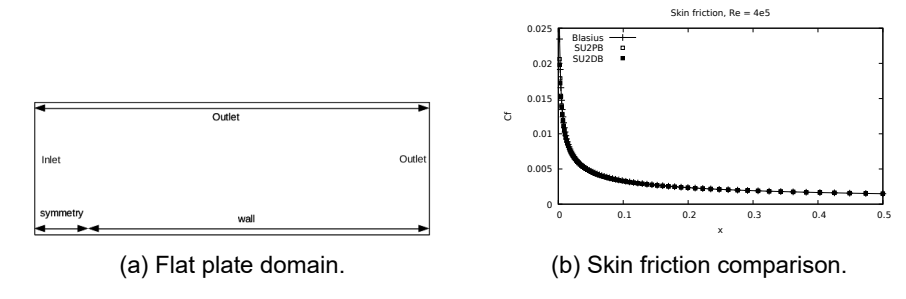


Figure 5: Flat plate domain (a) and skin friction comparison between numerical and Basius solution (b).

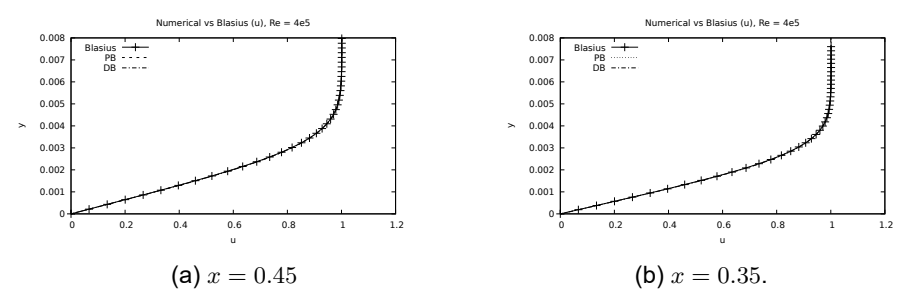


Figure 6: Comparison of x- component of velocity to the Blasius solution for laminar flow over a flatplate.

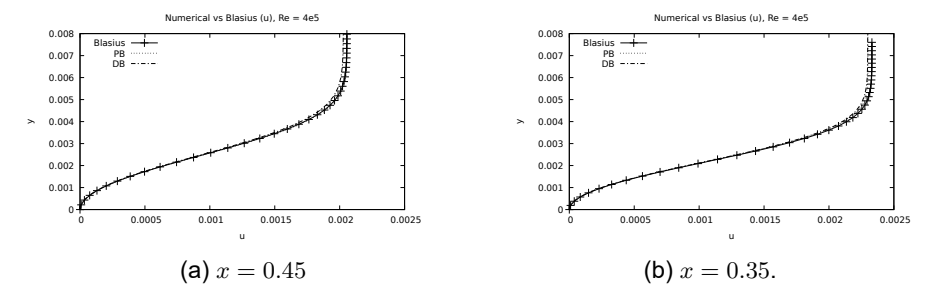


Figure 7: Comparison of y—component of velocity to the Blasius solution for laminar flow over a flatplate.

method does better than the density based method. Skin friction shows excellent agreement for both cases (Fig. 5b).

## 2.5.2 Laminar flow over a cylinder

A laminar flow over a cylinder is simulated for Re=40 and the resulting drag coefficient is plotted as a function of grid refinement. The simulations converge to a fixed value of  $C_d$  as the grid is refined (Fig. 8a). Fig. 8b shows the pressure coefficient along the cylinder for different grid resolutions which also converge upon grid refinement. The low Reynolds number is chosen to ensure the flow remains laminar and steady. The results in Fig. 8a obtained match closely with those obtained from other reference solutions[48].

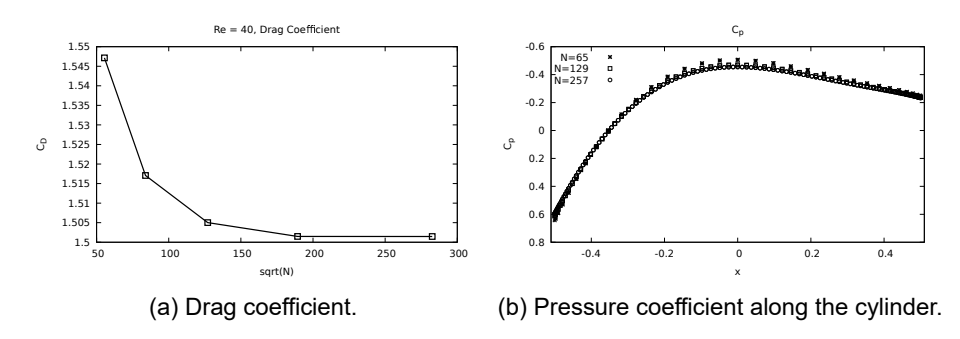


Figure 8: Laminar flow over a cylinder at Re = 40.

## 2.5.3 Inviscid flow over a NACA 0012 airfoil

Inviscid flow over a NACA 0012 hydrofoil at an angle of attack of 5° is simulated. This case is chosen to demonstrate the inviscid flow solver. The airfoil is placed in a rectangular channel and inclined at an angle of 5 degrees to the incoming flow. A flow tangency condition (i.e. free slip) is enforced on the surface of the airfoil. The boundary conditions used on the channel are inlet, outlet and free slip walls. This configuration of boundary conditions is necessary to ensure a unique solution from the solver. The streamlines and the pressure contours are shown in Fig. 9a and the distribution of the pressure coefficient over the hydrofoil is shown in Fig. 9b and compared to the results from RFOIL[8], a wind energy industry standard airfoil design tool. We observe good agreement between the inviscid version of the new pressure based method in SU2 and RFOIL.

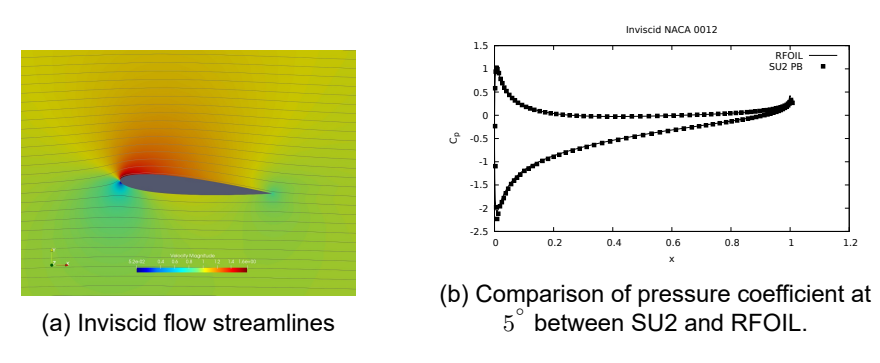


Figure 9: Results from inviscid flow over NACA 0012.

## 2.5.4 Laminar flow over a backward facing step

Flow over a backward facing step is a very popular validation problem and is commonly used to study the behavior of a numerical solver in separated flows. The domain consists of an inlet channel which expands into a larger channel across a step. The flow seperates at the step and re-attaches downstream along the lower wall. Depending on the Reynolds number, a secondary separated region can also occur along the top wall. We simulate a laminar flow over a backward facing step at Re=800 where flow is expected to separate along both the bottom and top walls. The numerical results compared to results from Gartling[49]. Step height is 0.5 units and the channel height is 1 unit.

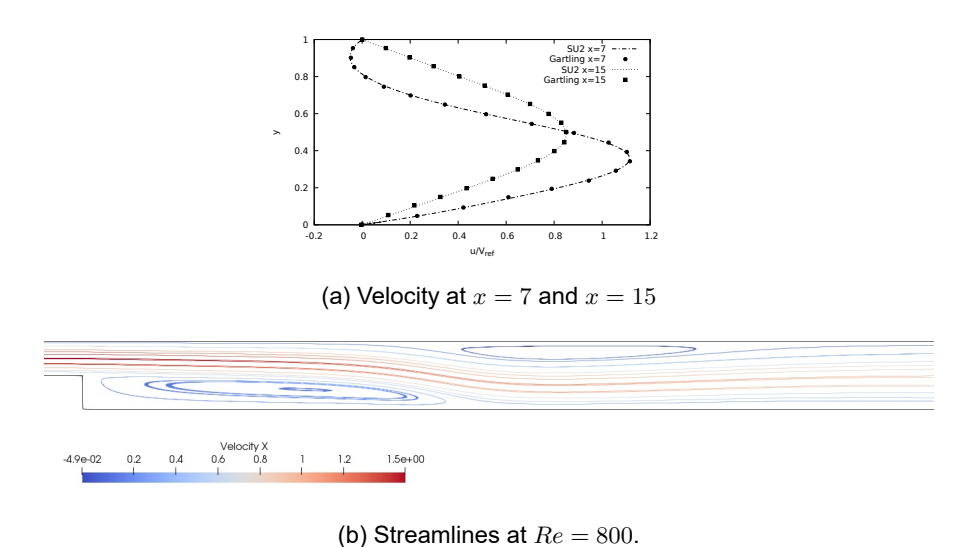


Figure 10: Laminar flow over a backward facing step. Comparison of velocity profiles obtained from the numerical results with the literature at two different x-locations (a) and streamlines showing the two recirculating zones along the bottom and top walls (b).

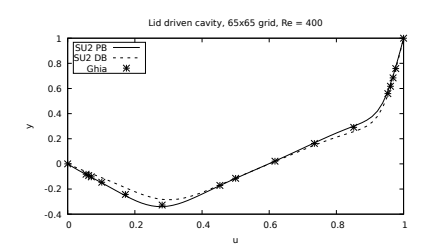
Fig. 10a compares the numerical and experimental results for the streamwise velocity component at two different locations. The velocity profile shows good agreement at both locations. The streamlines for a part of the domain are shown in 10b which clearly shows the two recirculating regions that are formed. The length of the recirculating zone along the lower wall is 5.81 units and along the upper wall is 5.69 units which match the results from [49].

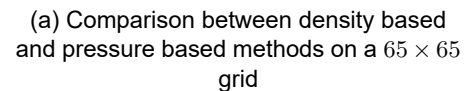
## 2.5.5 Lid driven cavity

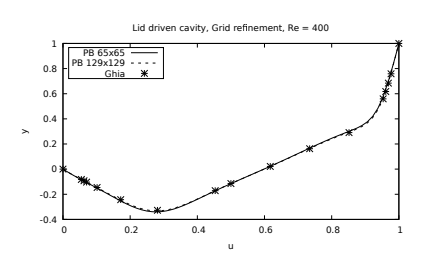
Flow within a lid-driven cavity is another classic validation problem in the CFD community. This case is chosen here to test the moving wall boundary condition. In this section, the results from a lid driven cavity is compared against benchmark results from Ghia[1]. The flow is fully laminar and at a Re=400. The domain consists of a unit square, where all four sides are treated as solid walls. The top wall is moving at a constant unit velocity in the x- direction. Results from the density based (DB) version and the newly implemented pressure based (PB) version are shown in Fig. 11a and results from two successively fine grids are shown in Fig. 11b. On the coarser  $(65\times65)$  grid, the PB method matches the reference solution more closely than the DB method. The difference between the reference solution and the PB solution improves upon grid refinement as expected.

## 2.5.6 Turbulent flow over a flat plate

A turbulent flow over a flat plate is simulated at Re=5e6 and the results compared to the standard 2D zero pressure gradient flat plate validation case from the NASA Turbulence Modeling resource[50]. The domain used is similar to the one shown in Fig. 5a, with more refinement in the wall normal direction to ensure adequate resolution of the turbulent boundary layer near the wall. The grids used are from the NASA turbulence modeling database and the coarsest grid has an average  $y+\approx 1.7$ .



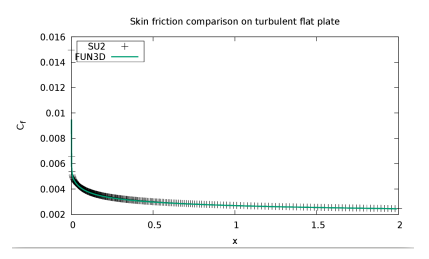


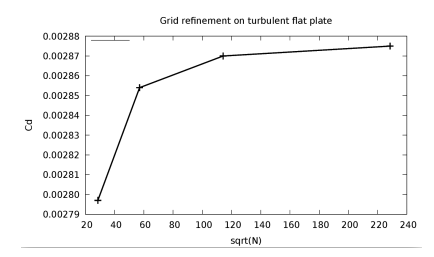


(b) Results from  $65 \times 65$  and  $129 \times 129$  grid with the pressure based method.

Figure 11: Comparison of the velocity profile obtained from pressure based (PB) and density based (DB) methods in SU2 and reference solution[1] along the centerline(x=0.5) for lid driven cavity, Re=400.

Subsequent grids are refined ensuring proper resolution of the boundary layer near the wall. Fig. 12a shows the comparison of skin friction obtained from the current pressure based method with the one obtained from FUN3D[50]. Fig. 12b shows the drag coefficient of the flat plate obtained for different grid resolutions. We observe that the drag coefficient converges to a single value upon grid refinement.





- (a) Skin friction comparison along the flatplate.
- (b) Drag coefficent with different grid resolutions.

Figure 12: Turbulent flow over a flat plate at Re = 5e6.

#### 2.5.7 Turbulent flow over NACA0012 airfoil

Flow over airfoils are a very typical problem in most aerodynamic applications. Lift and drag polars of airfoils used in the different sections of a wind turbine blade are commonly used as an input to the lower fidelity tools based on Blade Element Momemntum theory, lifting line theory, etc. which can then be used to analyze the performance of turbine blades. In this section, a fully turbulent flow over NACA0012 airfoil employing the SA and the SST turbulent models are compared with the experimental data[51] at a Re number of 6.0e6 on a grid with approximately 14000 elements. The pressure-based method matches the experimental data very closely (Fig. 13) at all angles of attack and also captures the maximum lift angle.

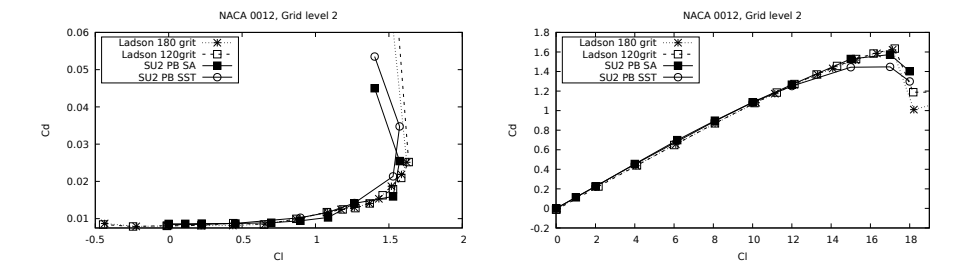


Figure 13: Turbulent flow over NACA0012 airfoil. A comparison of the numerical solution with the experimental data for lift to drag ratio (left) and lift coefficient for various angle of attacks (right).

## 3 Vortex Generator design

For this project the generic AVATAR 10 MW blade[52] is chosen as basis to apply and analyze the performance of the new vortex generators design. The details of this blade is summarized in the section below. LFTL performed the vortex generators design based on the blade data provided.

#### 3.1 AVATAR blade

The generic AVATAR blade is designed within the AVATAR project (FP7-ENERGY-2013-1/ no 608396) for research purposes. The blade is evaluated with the TNO's in-house Blade Optimization Tool (BOT) and the very tip section is excluded to fit the purpose of this project. The airfoil sections used for this blade is as follows (based on the AVATAR blade[52]):

Table 1: Airfoil sections used for the AVATAR rotor.

| Relative Thickness [%] | Airfoil     | Re                   | AoA  | Stagnation Point (x,y) |
|------------------------|-------------|----------------------|------|------------------------|
| 60.0                   | DU600       | $16.0 \times 10^{6}$ | 1.5  | 0.002908, -0.014254    |
| 39.6                   | DU396       | $16.0 \times 10^6$   | 2.5  | 0.006998, -0.024387    |
| 34.6                   | DU346       | $14.5 \times 10^{6}$ | 3.5  | 0.005666, 0.030618     |
| 30.0                   | DU 97-W-300 | $12.5 \times 10^{6}$ | 4.5  | 0.006684, -0.041905    |
| 24.0                   | DU240       | $8.5 \times 10^6$    | 10.5 | 0.006137, -0.05948     |

The DU600 is an artificial airfoil based on thickest available DU airfoil and DU240 is re-scaled to 24% relative thickness from DU 91-W2-250 airfoil.

The blade description including the chord, relative thickness and angle of attack is given in the following table:

Table 2: Blade description (based on the AVATAR rotor).

| Radius [m] | Chord [m] | Relative Thickness [%] | Angle of Attack [deg] |
|------------|-----------|------------------------|-----------------------|
| 1.76       | 5.38      | 0.99                   | 49.94                 |
| 3.83       | 5.38      | 0.99                   | 41.49                 |
| 5.90       | 5.46      | 0.97                   | 33.87                 |
| 7.97       | 5.56      | 0.93                   | 26.74                 |
| 10.04      | 5.66      | 0.86                   | 20.81                 |
| 12.11      | 5.76      | 0.78                   | 16.24                 |
| 14.18      | 5.87      | 0.70                   | 13.16                 |
| 16.25      | 6.02      | 0.63                   | 10.86                 |
| 18.31      | 6.13      | 0.56                   | 9.49                  |
| 20.38      | 6.21      | 0.51                   | 7.90                  |
| 22.45      | 6.23      | 0.47                   | 6.64                  |
| 24.52      | 6.20      | 0.44                   | 5.56                  |
| 26.59      | 6.14      | 0.42                   | 4.83                  |
| 28.66      | 6.06      | 0.40                   | 4.30                  |

| 30.73 | 5.97 | 0.38 | 4.11 |
|-------|------|------|------|
| 32.80 | 5.87 | 0.37 | 3.92 |
| 34.87 | 5.76 | 0.36 | 3.70 |
| 36.94 | 5.65 | 0.35 | 3.46 |
| 39.01 | 5.53 | 0.34 | 3.22 |
| 41.08 | 5.41 | 0.32 | 3.00 |
| 43.15 | 5.29 | 0.31 | 2.80 |
| 45.22 | 5.17 | 0.30 | 2.62 |
| 47.29 | 5.04 | 0.29 | 2.45 |
| 49.36 | 4.92 | 0.28 | 2.30 |
| 51.43 | 4.80 | 0.27 | 2.17 |
| 53.50 | 4.67 | 0.26 | 2.06 |
| 55.57 | 4.55 | 0.26 | 1.97 |
| 57.64 | 4.43 | 0.25 | 1.90 |
| 59.71 | 4.30 | 0.25 | 1.84 |
| 61.78 | 4.18 | 0.24 | 1.80 |
| 63.85 | 4.05 | 0.24 | 1.78 |
| 65.92 | 3.93 | 0.24 | 1.77 |
| 68.00 | 3.81 | 0.24 | 1.76 |
| 70.07 | 3.69 | 0.24 | 1.76 |
| 72.14 | 3.56 | 0.24 | 1.75 |
| 74.21 | 3.44 | 0.24 | 1.73 |
| 76.28 | 3.32 | 0.24 | 1.71 |
| 78.35 | 3.21 | 0.24 | 1.67 |
| 80.42 | 3.09 | 0.24 | 1.65 |
| 82.49 | 2.98 | 0.24 | 1.62 |
| 84.56 | 2.87 | 0.24 | 1.60 |
| 86.63 | 2.77 | 0.24 | 1.57 |
| 88.70 | 2.68 | 0.24 | 1.53 |
| 90.77 | 2.57 | 0.24 | 1.49 |
| 92.84 | 2.44 | 0.24 | 1.44 |
| 94.91 | 2.23 | 0.24 | 1.41 |
| 96.98 | 1.92 | 0.24 | 1.36 |
| 98.53 | 1.50 | 0.24 | 1.29 |
| 99.56 | 0.95 | 0.24 | 1.24 |
|       |      |      |      |

## 3.2 Design iterations

Laminar Flow Technology Limited (LFTL) made two major VG designs: co- and counter-rotating VGs (see Appendix A - D). Furthermore, initially each design had two different versions where the major difference were the sizes (especially the height) of the VGs. Since project budget was not enough to analyse the performance of all configurations, it is agreed with LFTL to select one configuration to performed the analysis. The advice of TNO was to choose a configuration with counter-rotating VGs since the literature indicates that this is the most effective between the two configurations. The choice between the design iterations for the counter-rotating VGs is left to LFTL. When analyzed in detailed, two iterations of counter-rotating VG designs had some missing



Figure 14: Sketch of the VG configuration showing the locations on AVATAR blade.

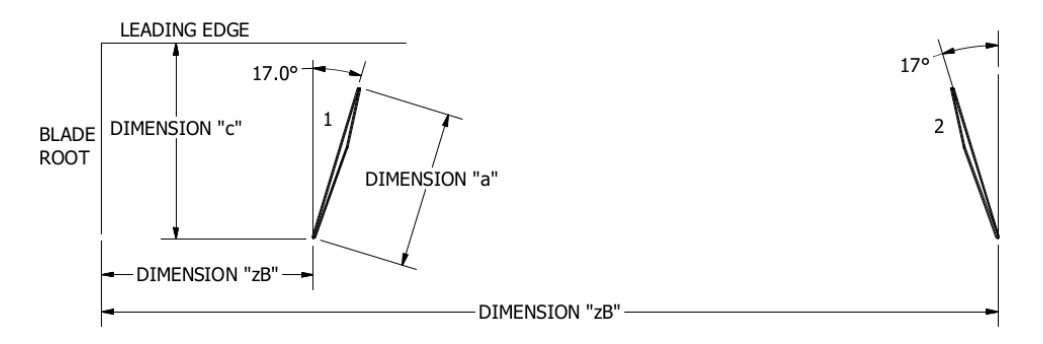


Figure 15: Sketch of the VG configuration detail iteration 1.

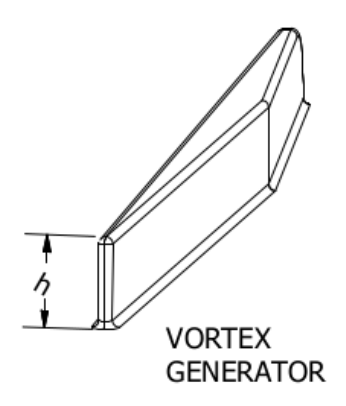


Figure 16: Sketch of the VG configuration detail iteration 1.

dimensions in order to generate a mesh (see Figures 15, 16, 17). LFTL delivered the final updated configuration for the counter-rotating VGs including the necessary dimensions for mesh generation (see Appendix E and Figure 18).

According to the final VG design configuration VGs span between 5.9m (approximately 5.9%) to 34.29m (approximately 34.3%) of the blade as sketched in Figure 14. According to this design VGs span 3 different airfoil sections namely DU600, DU396 and DU346. The other 2 airfoil sections (DU300 and DU240)) span the mid- to outboard regions of the blade are "clean" (no VGs on these sections).

## 3.2.1 Blade sections with VGs

Although there are around 34-35 VGs along the blade span it would be enough to simulate and obtain the lift and drag polars from a single VG placed on each different blade section to calculate the blade performance using the BOT. To this end the blade sections with VGs coinciding with the existing airfoil profiles are chosen for the sim-

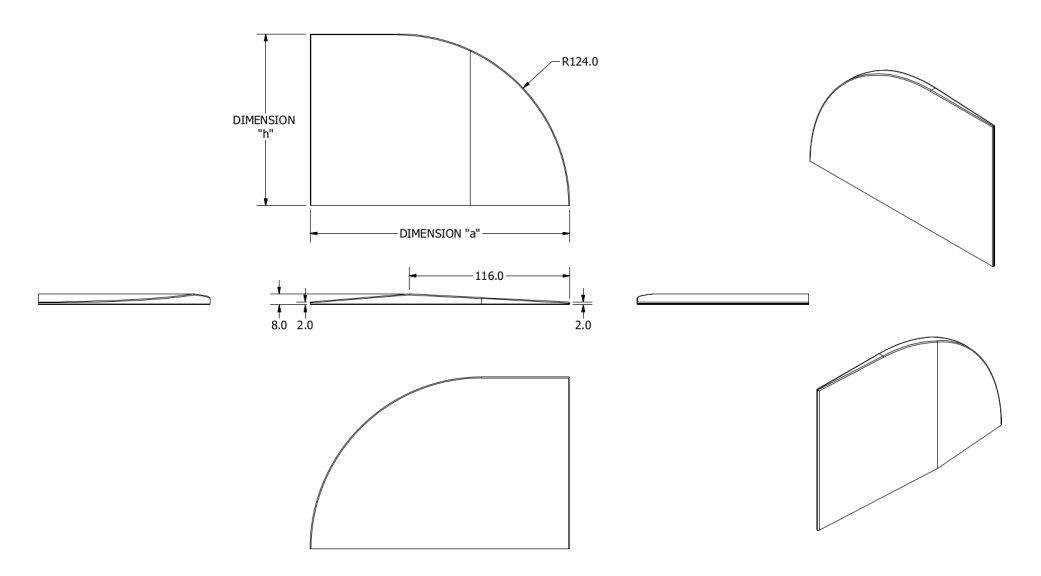


Figure 17: Sketch of the VG configuration detail iteration 2.

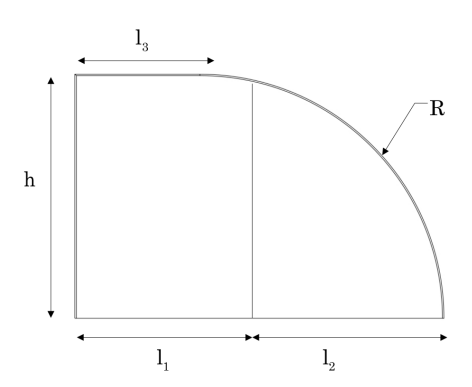


Figure 18: Final requested dimensions of the VG configuration detail iteration 2.

ulations. As mentioned in previous section these airfoil profiles are DU346, DU396 and DU600. The details of these airfoil sections together with the VG configuration is given in the following sections. Please note that, different than clean cases, since these airfoil sections involve designed VG configurations, the dimensions should be used either unscaled or scaled together with the VGs. In the project we used the unscaled dimensions.

### 3.2.1.1 DU346

VG station 33 coincides with DU346 profile. The exact thickness and chord length is found by interpolating the closest values. The final chord length of DU346 is 5.811m.

The corresponding VG dimensions are as follows:

- Height: h = 116mm
- Distance from leading edge: c = 1398mm
- $x_{vg}/c \approx 0.24$
- l1 = 108mm, l2 = 66mm, l3 = 58mm

- Length of VG: a = l1 + l2 = 174mm
- radius of curvature of VG leading edge: R = 116mm
- $\beta=17^\circ$  (angle between VG and the free-stream flow)

#### 3.2.2 DU396

VG station 27 coincides with DU396 profile. The exact thickness and chord length is found by interpolating the closest values. The final chord length of DU346 is 6.087m.

The corresponding VG dimensions are as follows:

- Height: h = 121mm
- Distance from leading edge: c = 1272mm
- $x_{vq}/c \approx 0.2$
- l1 = 112mm, l2 = 70mm, l3 = 61mm
- Length of VG: a = l1 + l2 = 182mm
- radius of curvature of VG leading edge: R=121mm
- $\beta = 17^{\circ}$

#### 3.2.3 DU600

VG station 14 coincides with DU600 profile. The exact thickness and chord length is found by interpolating the closest values. The final chord length of DU346 is 6.03m.

The corresponding VG dimensions are as follows:

- Height: h = 119mm
- Distance from leading edge: c = 1436mm
- $x_{vg}/c \approx 0.23$
- l1 = 111mm, l2 = 68mm, l3 = 60mm
- Length of VG: a = l1 + l2 = 179mm
- radius of curvature of VG leading edge: R = 119mm
- $\beta = 17^{\circ}$

## 4 Mesh topology

#### 4.1 Airfoil sections without VG

A two dimensional mesh is used for simulations without VG (see e.g. Figure 19). Initial cell height is chosen based on the highest Re number for each airfoil. For the highest Re numbers, a  $y^+ < 5$  is maintained in all cases. At lower Re numbers, a minimum  $y^+ < 1$  naturally arises. The expansion ratio of cells in boundary layer is 1.08. Nodes are clustered near the trailing edge, leading edge and other portions with significant curvature as shown in Figure 20.

2D airfoil sections contain 260 (DU240) to 350 (DU600) points along the airfoil surface depending on the airfoil thickness, with a maximum included angle  $151^{\circ}$ , skewness of 0.68. Total number of grid points for these 2D meshes are around 50,000. The domain extends for approximately 150 chord lengths.

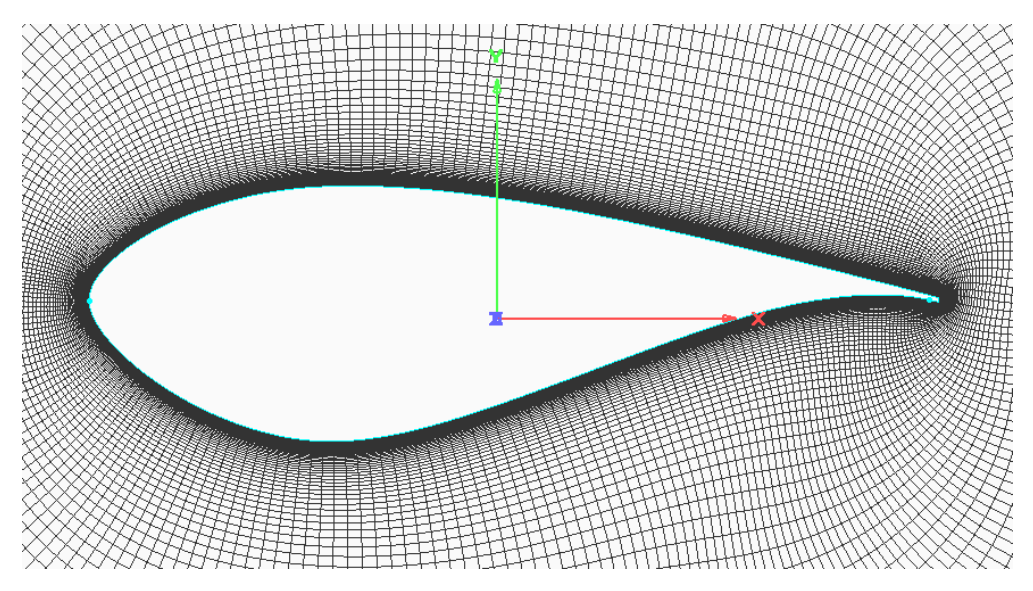


Figure 19: DU300 2d mesh of the airfoil (left) and zoomed into the BL (right).

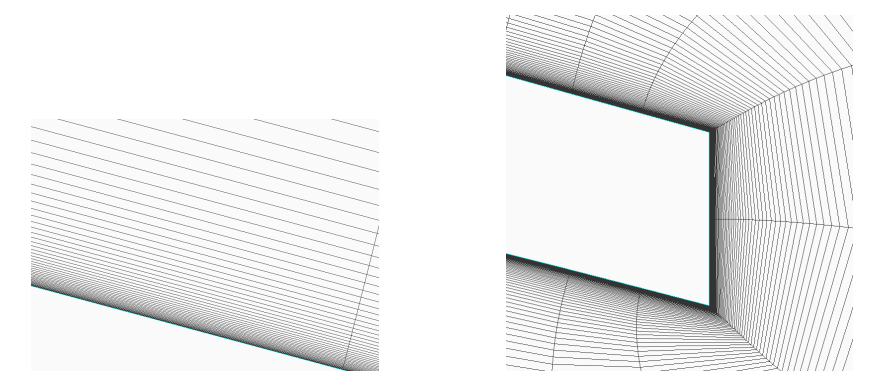


Figure 20: Details of the DU300 mesh. Boundary layer (left) and Trailing edge (right).

#### 4.2 Airfoil sections with VG

As mentioned in the previous sections the airfoil sections containing VG are DU346, DU396 and DU600. In this section the mesh topology details of these sections with VGs are presented.

For the CFD simulations it is assumed that the VG with the given configuration is aligned as an infinitely long counter-rotating pairs as shown in Figure 21. Furthermore a single VG is isolated and placed on a strip of an airfoil section where *symmetry* boundary conditions are applied on both boundaries in the span direction which is shown as blue dotted lines in Figure 21. In this way, a single VG can be simulated which is computationally less expensive and also the isolated lift and drag polars can be obtained to be an input for BOT simulations.

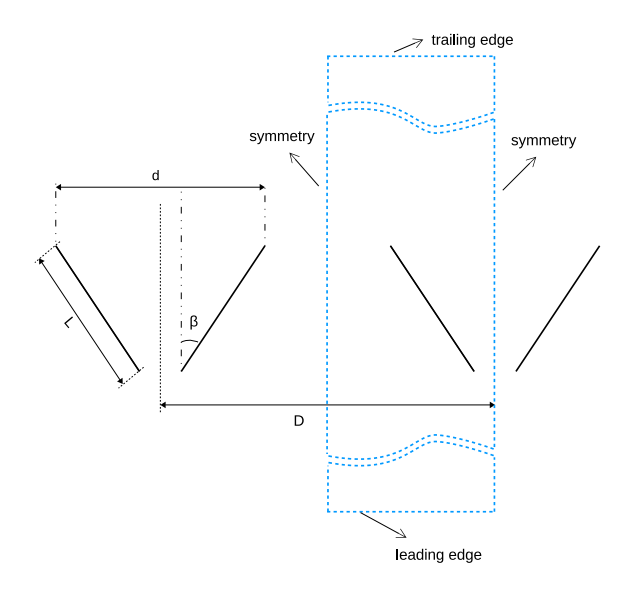


Figure 21: A sketch of a counter-rotating VG orientation and placement on an extruded airfoil section (blue region). Top view.

A fully hexahedral mesh is generated for all cases. A  $y+\approx 1$  is maintained based on the operating Re numbers for each airfoil section. The domain extends for approximately 100 chord lengths for each airfoil ( $\approx 600m$ ).

#### 4.2.1 DU346

The initial cell height is  $\approx 6 \times 10^{-6}$ . There are 1020 points on the airfoil surface and the maximum included angle is  $144^{\circ}$ . The total number of grid points is =4,781,070. The mesh topology is presented in Figure 22.

#### 4.2.2 DU396

The initial cell height is  $\approx 7 \times 10^{-6}$ . There are 1097 points on the airfoil surface and the maximum included angle is  $150^{\circ}$ . The total number of grid points is =5,001,150. The mesh topology is presented in Figure 23.

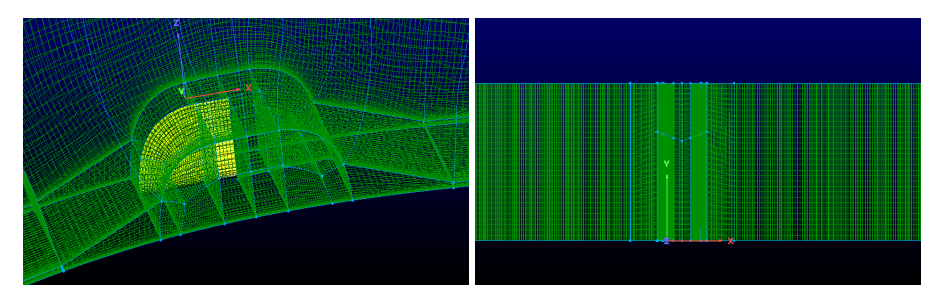


Figure 22: DU346 mesh topology around VG (right) and top view showing orientation (left).

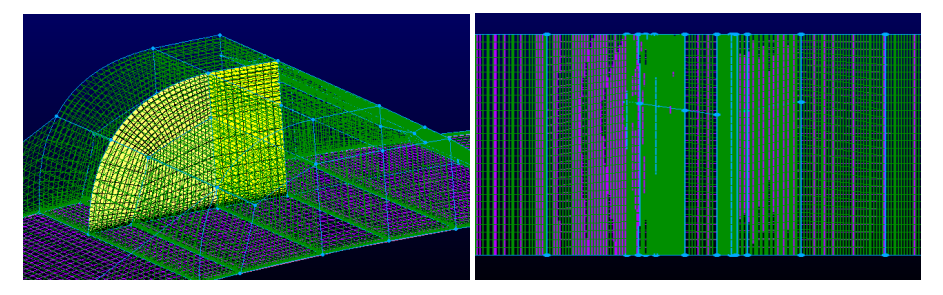


Figure 23: DU396 mesh topology around VG (right) and top view showing orientation (left).

## 4.2.3 DU600

The initial cell height is  $\approx 9 \times 10^{-6}$ . There are 1044 points on the airfoil surface and the maximum included angle is  $144^{\circ}$ . The total number of grid points is =5,253,600. The mesh topology is presented in Figure 24.

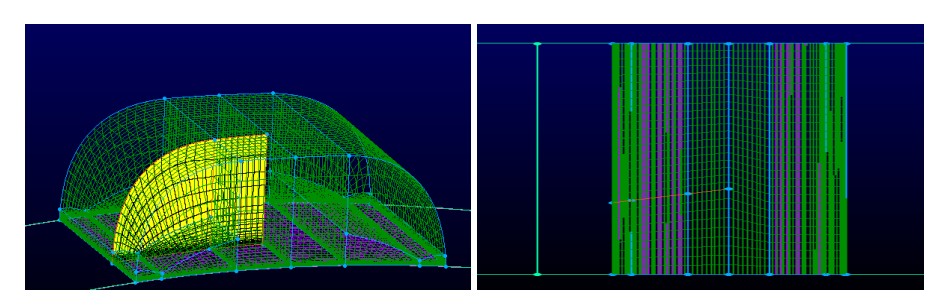


Figure 24: DU600 mesh topology around VG (right) and top view showing orientation (left).

## 5 Simulation Results of Airfoil Sections for Clean and VG Cases

## 5.1 Mesh refinement study

For the clean airfoil, a grid refinement study is carried out on DU 97-W-300 airfoil that is extruded towards the span (y) direction at  $AoA=2.5^{\circ}$ . The chord length of the airfoil is 0.65m. The coarsest grid has 128 points, the reference grid has 300 points and the finest grid has 512 points on the airfoil and 4 points in the span direction.

Figure 25 shows the pressure coefficient and skin friction coefficient along the airfoil obtained from the three grids. The results from reference grid and fine grid are mostly identical and thus the reference grid (properties) will be used for further computations.

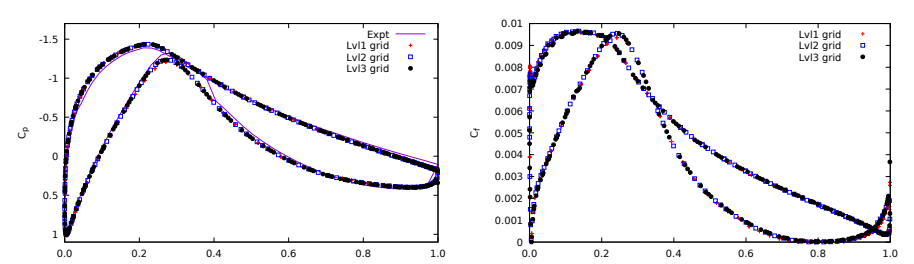


Figure 25: Comparison of the pressure coefficient (left) and the skin friction coefficient (right) at an  $AoA = 2.5^{\circ}$ ,  $Re = 2.0 \times 10^{6}$  for different grid resolutions.

#### 5.2 Clean airfoil sections

## 5.2.1 Validation case

Before going into the simulation results for individual airfoil sections a validation case is presented for a clean airfoil case briefly. A fully turbulent flow over the DU 97-W-300 airfoil at  $Re=2\times 10^6$  is considered. Figure 26 shows the lift and drag polars from SU2 and the experimental data from Baldaccino[53]. Additionally, the lift data from other CFD methods obtained from Avatar report[52] is also given. The maximum lift angle and the maximum  $C_l$  is over estimated by CFD compared to experiments. However, the results from SU2 are in close agreement to those reported by other CFD methods in AVATAR. Similar behavior is observed for  $C_d$  as well. The results presented in the validation section is taken from the publication on estimating the effect of leading edge erosion on wind turbine blades[54].

#### 5.2.2 Simulation matrix

For the clean airfoil sections the cases simulated are given in Tables 3 and 4. For each case 3 different Re numbers are considered including the design Re number. The lift and drag polar is obtained by considering selected angles of attack where some extra simulations are performed around the design angle of attack. These extra angles of attack around the design angle of attack are necessary for BOT simulations since including the VGs would change the design angle of a given airfoil section.

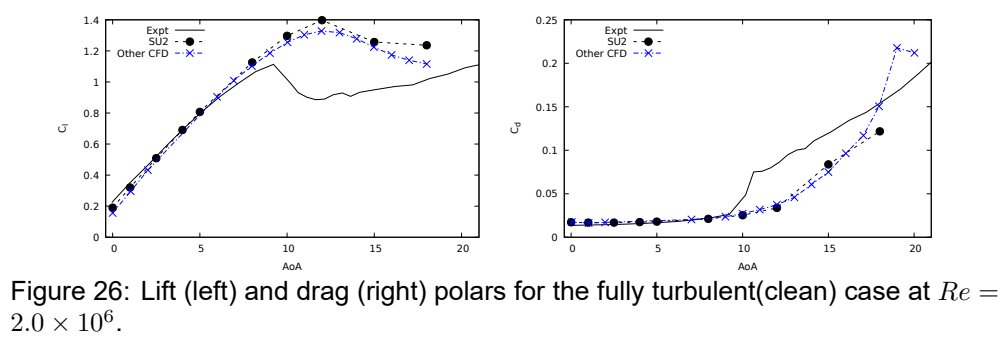


Table 3: Simulation matrix for the clean cases.

|     |       | DU240 |        |       | DU300 |        |       | DU346 |        |
|-----|-------|-------|--------|-------|-------|--------|-------|-------|--------|
| Re  | 2.0e6 | 9.0e6 | 16.0e6 | 2.0e6 | 9.0e6 | 16.0e6 | 2.0e6 | 8.0e6 | 14.5e6 |
| AoA | 0.0   | 0.0   | 0.0    | 0.0   | 0.0   | 0.0    | 0.0   | 0.0   | 0.0    |
|     | 1.0   | 1.0   | 1.0    | 1.0   | 1.0   | 1.0    | -     | -     | -      |
|     | 1.5   | 1.5   | 1.5    | -     | -     | -      | -     | -     | -      |
|     | 2.0   | 2.0   | 2.0    | -     | -     | -      | 2.0   | 2.0   | 2.0    |
|     | -     | -     | -      | 2.5   | 2.5   | 2.5    | -     | -     | -      |
|     | -     | -     | -      | -     | -     | -      | 3.0   | 3.0   | 3.0    |
|     | -     | -     | -      | -     | -     | -      | 3.5   | 3.5   | 3.5    |
|     | 4.0   | 4.0   | 4.0    | 4.0   | 4.0   | 4.0    | 4.0   | 4.0   | 4.0    |
|     | -     | -     | 5.0    | 5.0   | 5.0   | 5.0    | -     | -     | -      |
|     | 6.0   | 6.0   | 6.0    | -     | -     | -      | 6.0   | 6.0   | 6.0    |
|     | -     | -     | 8.0    | 8.0   | 8.0   | 8.0    | -     | -     | -      |
|     | 10.0  | 10.0  | 10.0   | 10.0  | 10.0  | 10.0   | 10.0  | 10.0  | 10.0   |
|     | 12.0  | 12.0  | 12.0   | 12.0  | 12.0  | 12.0   | 12.0  | 12.0  | 12.0   |
|     | -     | -     | -      | 13.0  | 13.0  | 13.0   | -     | -     | -      |
|     | 15.0  | 15.0  | 15.0   | 15.0  | 15.0  | -      | 15.0  | 15.0  | 15.0   |
|     | -     | -     | 18.0   | 18.0  | 18.0  | 18.0   | -     | -     | -      |
|     | -     | -     | 20.0   | -     | -     | -      | -     | -     | -      |

Table 4: Simulation matrix for the clean cases.

|     |       | DU396 |        |       | DU600 |       |
|-----|-------|-------|--------|-------|-------|-------|
| Re  | 2.0e6 | 7.0e6 | 12.5e6 | 2.0e6 | 5.0e6 | 8.5e6 |
| AoA | 0.0   | 0.0   | 0.0    | 0.0   | 0.0   | 0.0   |
|     | 2.0   | 2.0   | 2.0    | 2.0   | 2.0   | 2.0   |
|     | 4.0   | 4.0   | 4.0    | -     | -     | -     |
|     | 4.5   | 4.5   | 4.5    | -     | -     | -     |
|     | 5.0   | 5.0   | 5.0    | -     | -     | -     |
|     | 6.0   | 6.0   | 6.0    | 6.0   | 6.0   | 6.0   |
|     | -     | -     | -      | 8.0   | 8.0   | 8.0   |
|     | -     | -     | -      | 8.5   | 8.5   | 8.5   |
|     | -     | -     | -      | 9.0   | 9.0   | 9.0   |
|     | 10.0  | 10.0  | 10.0   | 10.0  | 10.0  | 10.0  |
|     | 12.0  | 12.0  | 12.0   | 12.0  | 12.0  | 12.0  |
|     | 15.0  | 15.0  | 15.0   | 15.0  | 15.0  | 15.0  |

#### 5.3 Simulation results

SU2 simulations are performed with the newly developed pressure-based incompressible Navier-Stokes solver. Both clean and VG cases are run until a convergence is obtained or the residuals dropped at least 2 orders although in very few cases (e.g. DU600 for lower angle of attacks) this convergence was not achieved as intended. Fully turbulent conditions are assumed in all the runs. Since encouraging results were observed in 26, in this iteration SU2 simulations are performed with the SA turbulence model.

RFOIL is an TNO in-house 2D aerodynamic design and performance analysis tool that is developed based an earlier version of XFOIL. It is modified for wind turbine airfoil sections and extended to include rotational effects as well.

Two numerical solutions are compared in this section and in general it is not possible to argue if one numerical solution is better then the other. But, the main point is to demonstrate that results obtained by two different numerical methods are closer to each other for these two airfoil sections. The main strategy for analyzing the performance of the blade is to compare the SU2 CFD simulations obtained for a clean blade with the one for a blade with VGs. In this case, the comparison will be meaningful as long as the numerical simulations are converged.

In this section a selection of numerical results obtained by both SU2 CFD simulations and RFOIL are presented for each airfoil sections. Comparison shows that lift and drag polars between SU2 and RFOIL for thinner airfoil sections (DU240 and DU300) are in better agreement in the linear regions up until around  $10^{\circ}$  (Figures 28 - 29 and 34 - 35). After the linear region both numerical simulations deviate from each other slightly which holds true both for lift and drag polars. When the distribution of pressure coefficients at various Re numbers and angle of attacks are compared for the same two airfoil sections (Figures 31, 32, 37 and 38) it can be seen that these results are in a very good agreement.

Although the results obtained for DU346 do not match as well as the thinner airfoil sections, both numerical methods show similar trends for lift and drag polars as well as the pressure coefficient distributions (Figures 40 - 44). Around (or just before) design angle of  $3.5^{\circ}$  RFOIL lift values show a sudden drop which happens for both the numerical simulations for DU396 airfoil section (Figures 46 - 48). This abrupt drop is not observed in the drag polars of these numerical results.

The convergence of the SU2 simulations for DU600 airfoil section were slightly poorer then for the other sections, especially for lower angles of attack. RFOIL did not converge at all for DU600 when run with the fully turbulent mode and with the natural transition mode some of the angles of attacks did not converge. In the Figures between 52 and 56 the SU2 results that are obtained for turbulent flow conditions are compared with the RFOIL results for transitional flow conditions to give an indication about both solutions. It is interesting to see that both SU2 and RFOIL pressure

coefficient distributions show very similar trends where both cases suggest a large separation regions (see Figures 55 and 56).

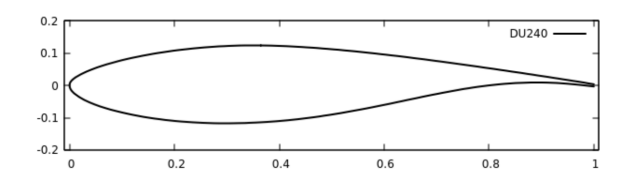


Figure 27: DU 97-W-240 airfoil profile.

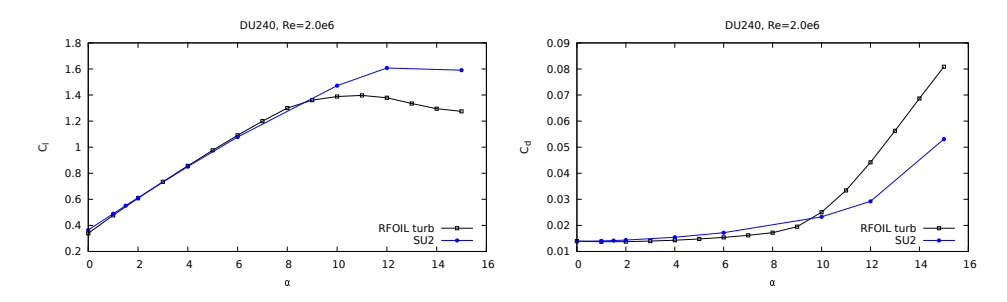


Figure 28: A comparison of lift (left) and drag (right) polar for DU240 for  $Re = 2.0 \times 10^6$  obtained from Rfoil and SU2 numerical simulations.

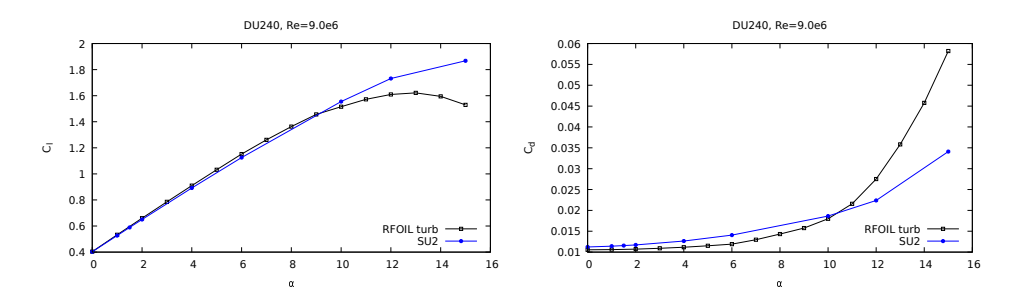


Figure 29: A comparison of lift (left) and drag (right) polar for DU240 for  $Re = 9.0 \times 10^6$  obtained from Rfoil and SU2 numerical simulations.

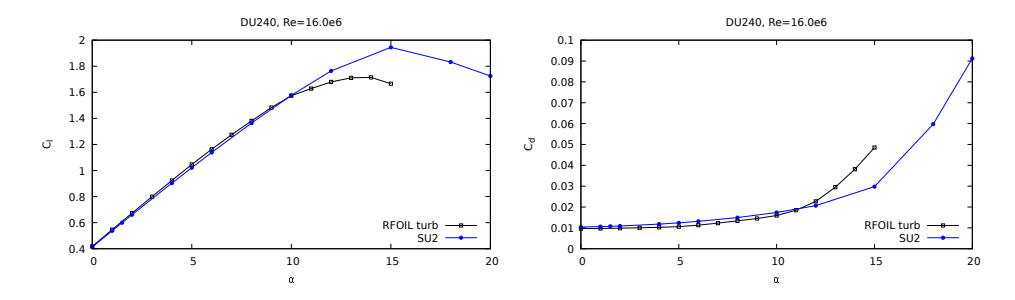


Figure 30: A comparison of lift (left) and drag (right) polar for DU240 for  $Re=16.0\times10^6$  obtained from Rfoil and SU2 numerical simulations.

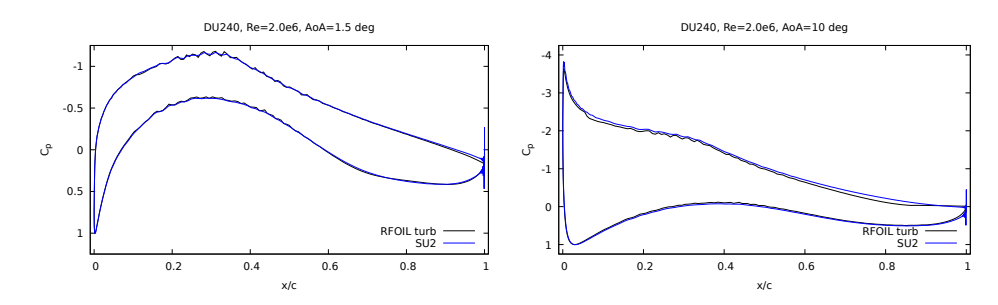


Figure 31: A comparison of pressure coefficients (Cp) for a Re number of  $2.0 \times 10^6$  for  $1.5^{\circ}$  (design angle of attack) and  $10^{\circ}$  for DU240.

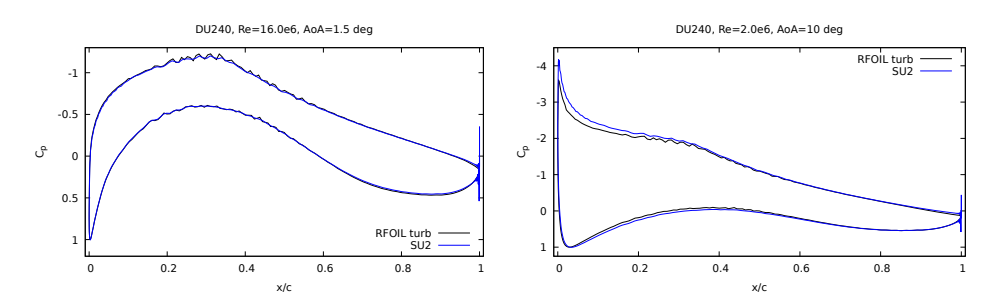


Figure 32: A comparison of pressure coefficients (Cp) for the design Re number of  $16.0\times10^6$  for  $1.5^\circ$  (design angle of attack) and  $10^\circ$  for DU240.

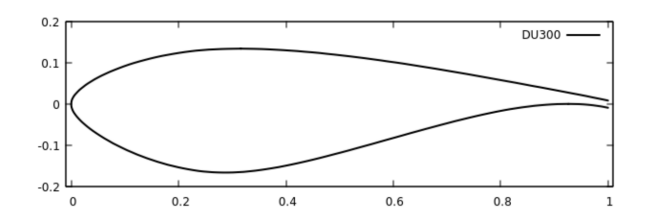


Figure 33: DU 97-W-300 airfoil profile.

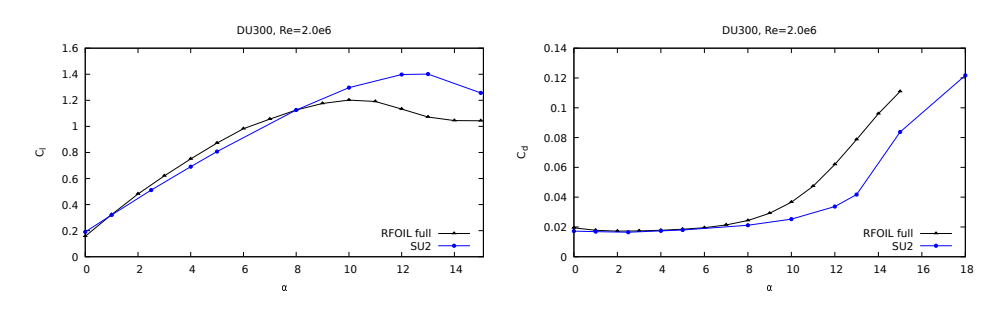


Figure 34: A comparison of lift (left) and drag (right) polar for DU300 for  $Re=2.0\times10^6$  obtained from Rfoil and SU2 numerical simulations.

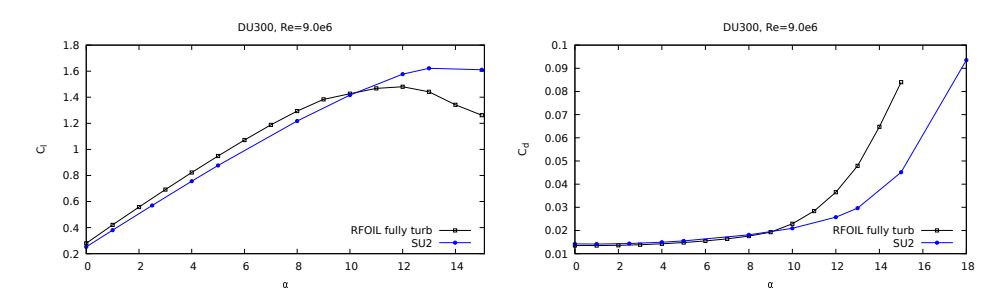


Figure 35: A comparison of lift (left) and drag (right) polar for DU300 for  $Re=9.0\times10^6$  obtained from Rfoil and SU2 numerical simulations.

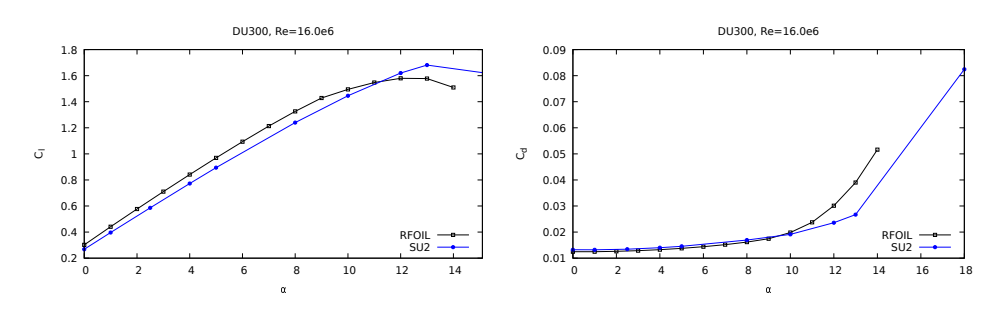


Figure 36: A comparison of lift (left) and drag (right) polar for DU300 for  $Re=16.0\times10^6$  obtained from Rfoil and SU2 numerical simulations.

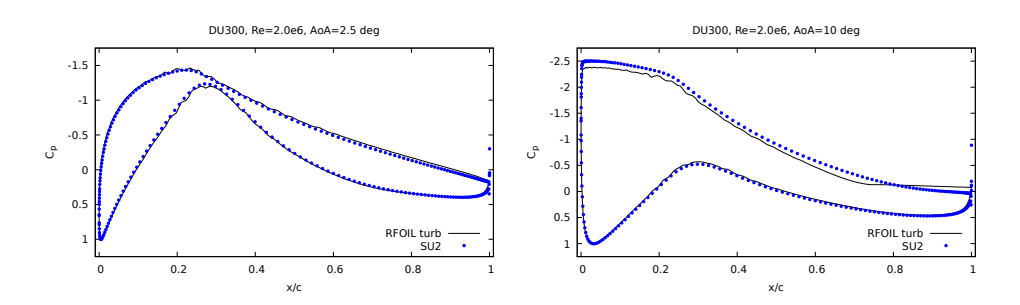


Figure 37: A comparison of pressure coefficients (Cp) for a Re number of  $2.0\times10^6$  for  $2.5^\circ$  (design angle of attack) and  $10^\circ$  for DU300.

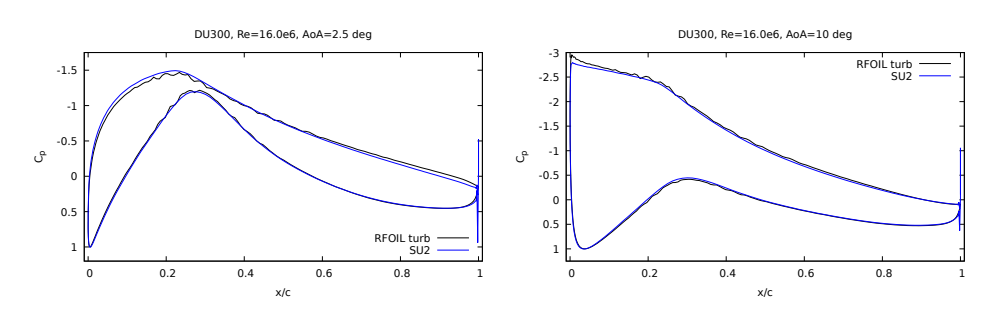


Figure 38: A comparison of pressure coefficients (Cp) for the design Re number of  $16.0\times10^6$  for  $2.5^\circ$  (design angle of attack) and  $10^\circ$  for DU300.

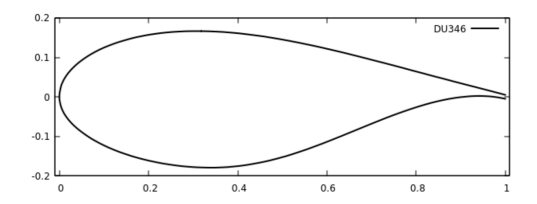


Figure 39: DU 97-W-346 airfoil profile.

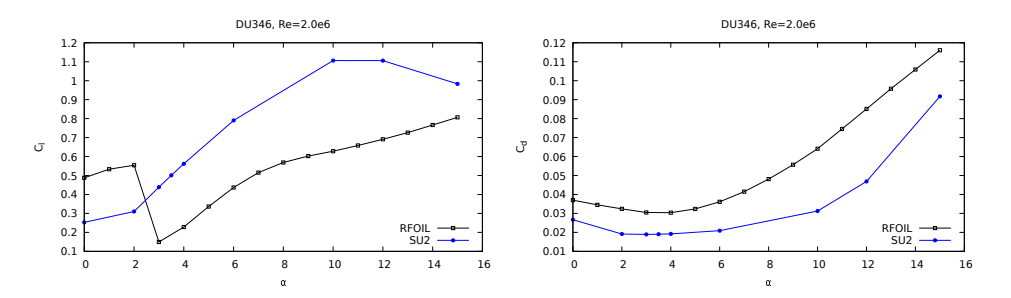


Figure 40: A comparison of lift (left) and drag (right) polar for DU346 for  $Re = 2.0 \times 10^6$  obtained from Rfoil and SU2 numerical simulations.

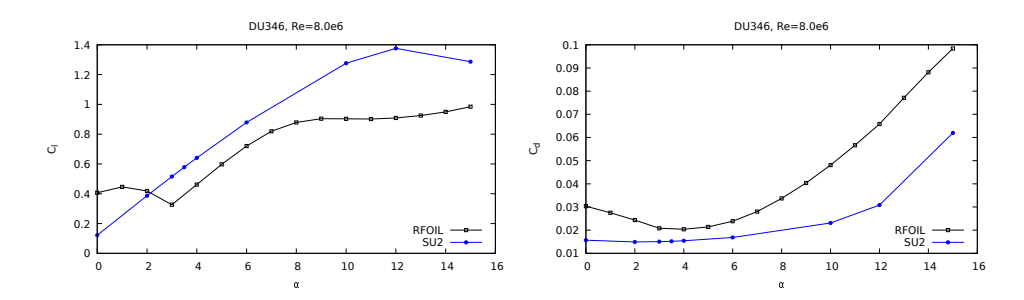


Figure 41: A comparison of lift (left) and drag (right) polar for DU346 for  $Re = 8.0 \times 10^6$  obtained from Rfoil and SU2 numerical simulations.

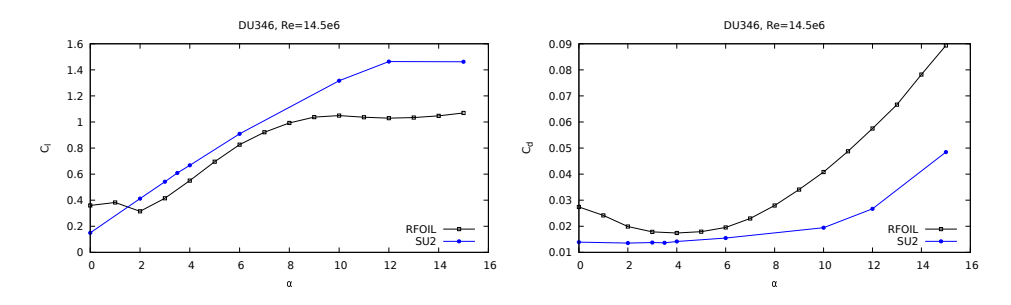


Figure 42: A comparison of lift (left) and drag (right) polar for DU346 for  $Re=14.5\times10^6$  obtained from Rfoil and SU2 numerical simulations.

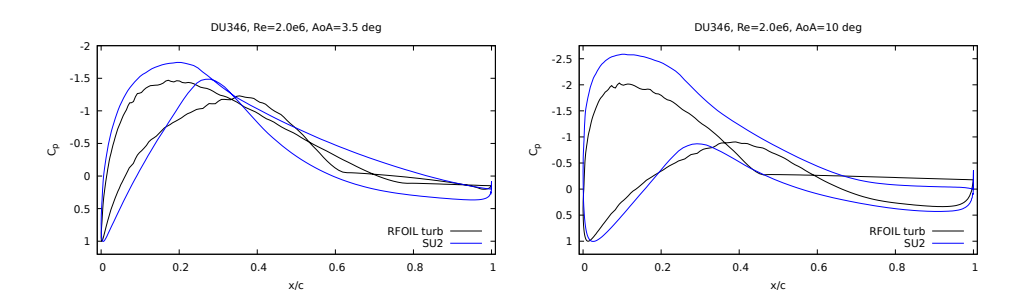


Figure 43: A comparison of pressure coefficients (Cp) for a Re number of  $2.0 \times 10^6$  for  $3.5^{\circ}$  (design angle of attack) and  $10^{\circ}$  for DU346.

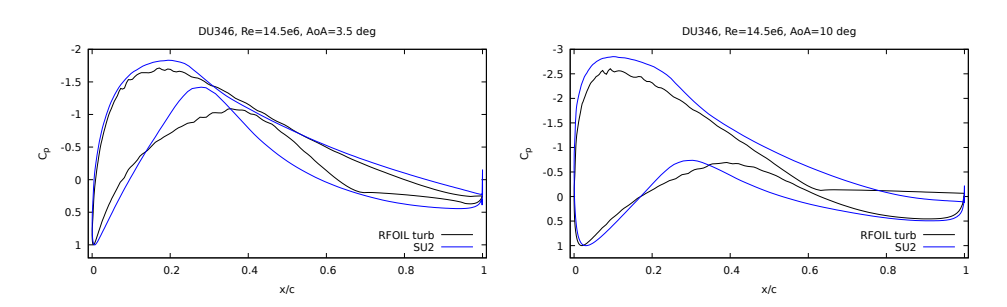


Figure 44: A comparison of pressure coefficients (Cp) for the design Re number of  $14.5\times10^6$  for  $3.5^\circ$  (design angle of attack) and  $10^\circ$  for DU346.

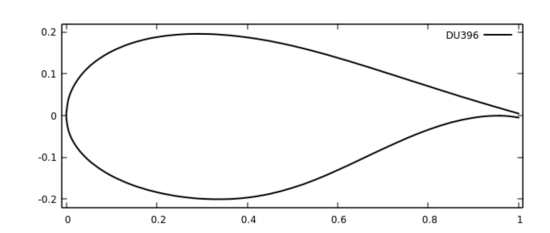


Figure 45: DU 97-W-396 airfoil profile.

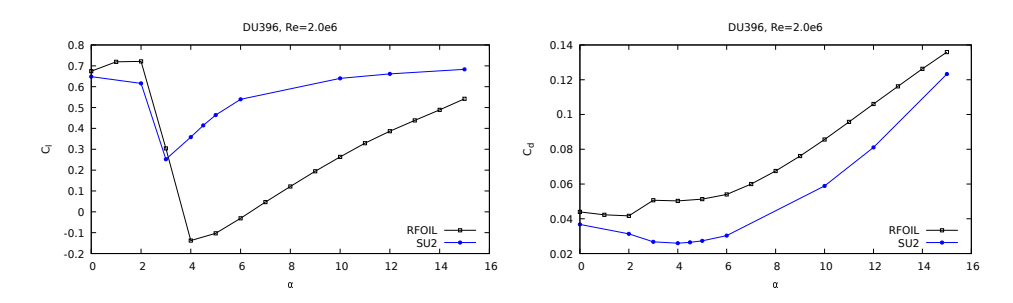


Figure 46: A comparison of lift (left) and drag (right) polar for DU396 for  $Re=2.0\times10^6$  obtained from Rfoil and SU2 numerical simulations.

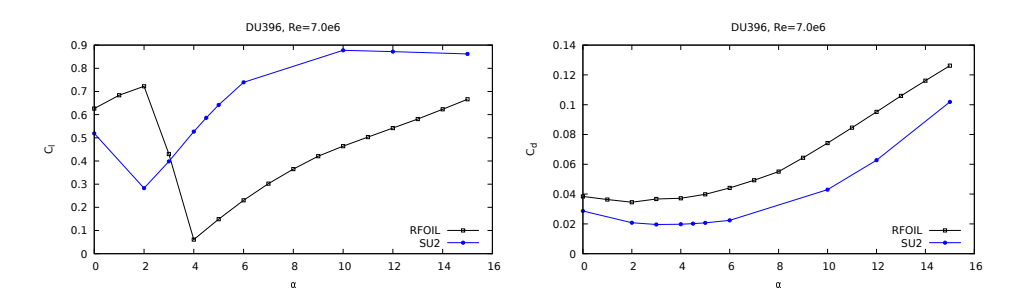


Figure 47: A comparison of lift (left) and drag (right) polar for DU396 for  $Re=2.0\times10^6$  obtained from Rfoil and SU2 numerical simulations.

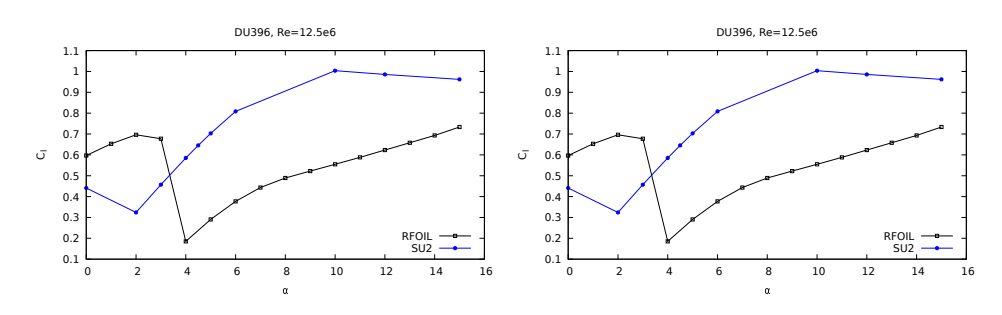


Figure 48: A comparison of lift (left) and drag (right) polar for DU396 for  $Re=12.5\times10^6$  obtained from Rfoil and SU2 numerical simulations.

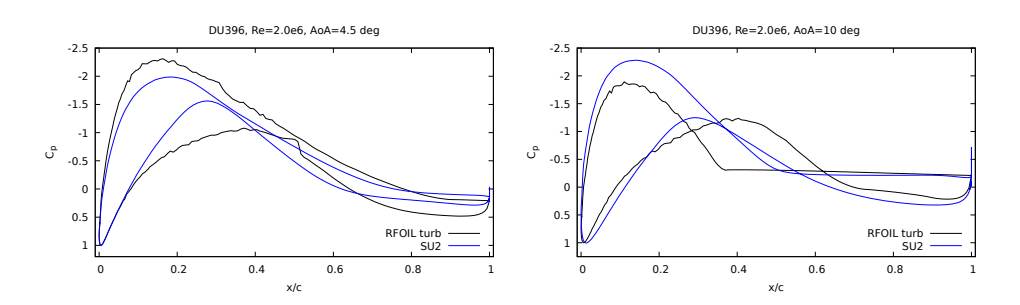


Figure 49: A comparison of pressure coefficients (Cp) for a Re number of  $2.0\times10^6$  for  $4.5^\circ$  (design angle of attack) and  $10^\circ$  for DU396.

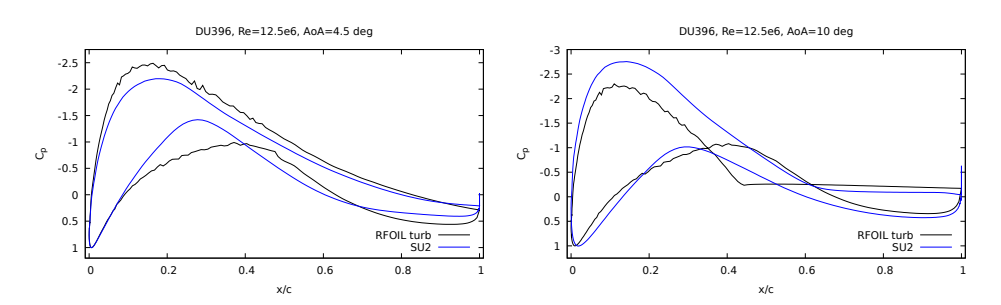


Figure 50: A comparison of pressure coefficients (Cp) for the design Re number of  $12.5\times10^6$  for  $4.5^\circ$  (design angle of attack) and  $10^\circ$  for DU396.

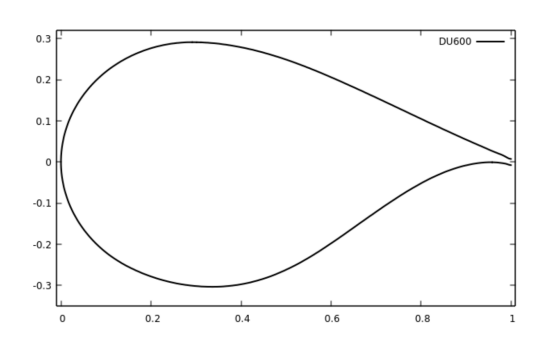


Figure 51: DU 97-W-600 airfoil profile.

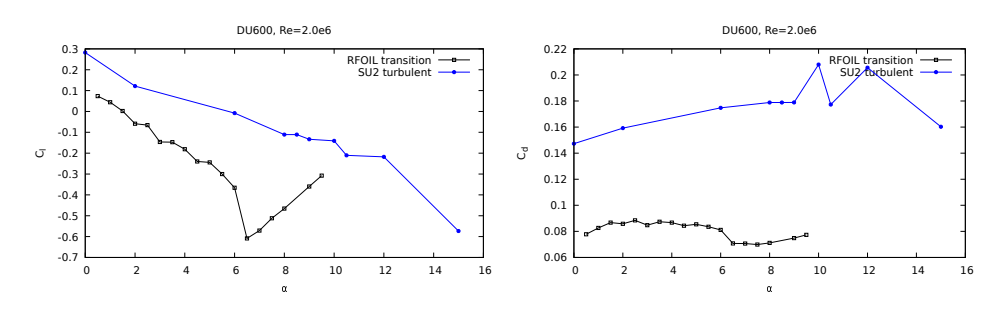


Figure 52: A comparison of lift (left) and drag (right) polar for DU600 for  $Re = 2.0 \times 10^6$  obtained from Rfoil and SU2 numerical simulations.

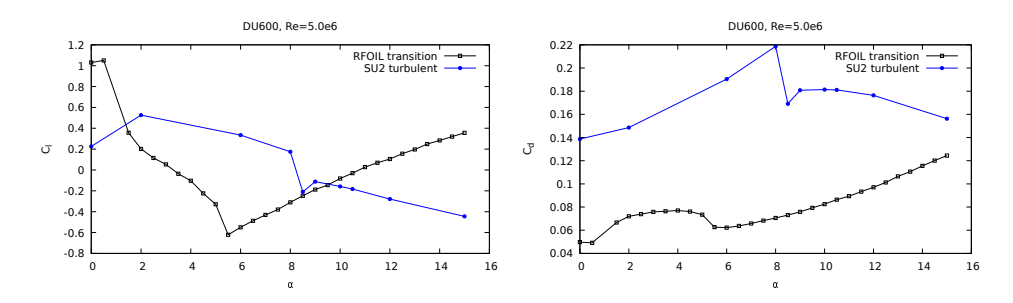


Figure 53: A comparison of lift (left) and drag (right) polar for DU600 for  $Re = 5.0 \times 10^6$  obtained from Rfoil and SU2 numerical simulations.

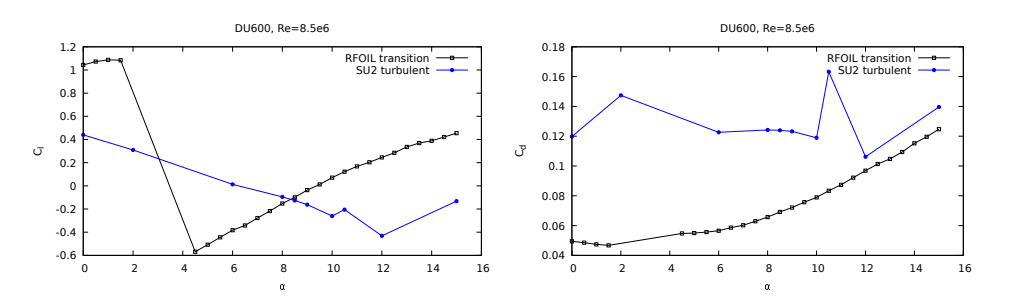


Figure 54: A comparison of lift (left) and drag (right) polar for DU600 for  $Re=8.5\times10^6$  obtained from Rfoil and SU2 numerical simulations.

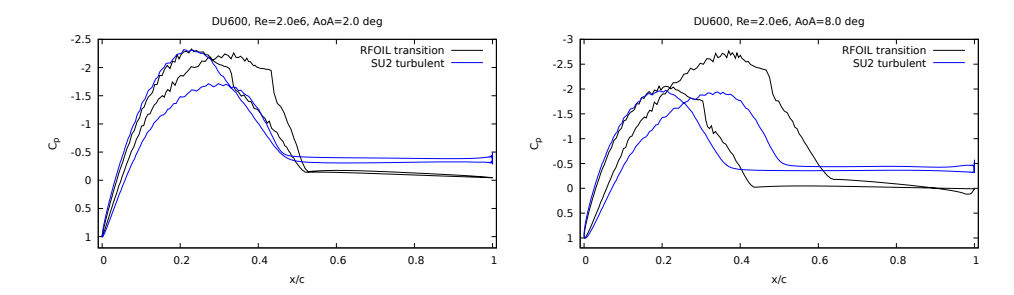


Figure 55: A comparison of pressure coefficients (Cp) for a Re number of  $2.0\times10^6$  for  $2^\circ$  and  $8.0^\circ$  for DU600.

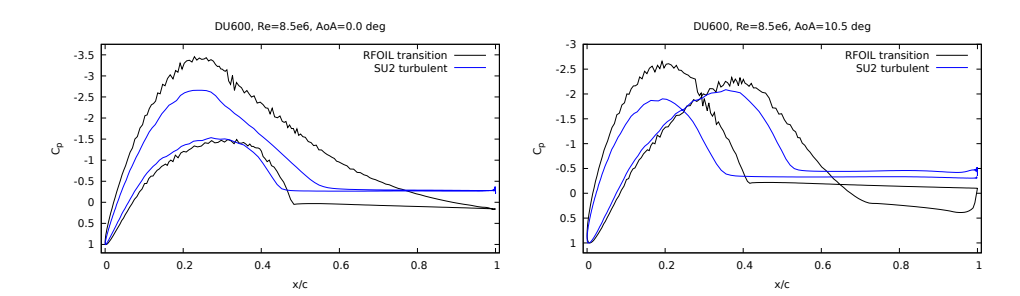


Figure 56: A comparison of pressure coefficients (Cp) for the design Re number of  $8.5\times10^6$  for  $0^\circ$  and  $10.5^\circ$  (design angle of attack) for DU600.

#### 5.4 Airfoil sections with a VG

In this section the method and results for the numerical simulations of airfoil sections with VGs are presented. Unlike clean airfoils, VG simulations are performed on a strip of an airfoil section where the airfoil section is extruded in the span direction. VG is placed on this strip as described in previous sections leading to a three-dimensional flow structure. Although lift and drag polars from this configuration leads to single curves the distribution of the pressure coefficient, Cp, varies at each x-z plane along the y-direction. Thus, instead of averaging, the Cp curves are presented at selected y- locations as indicated in Figure 57. These locations correspond to mid of airfoil strip, both edges of the VG and the mid of the VG.

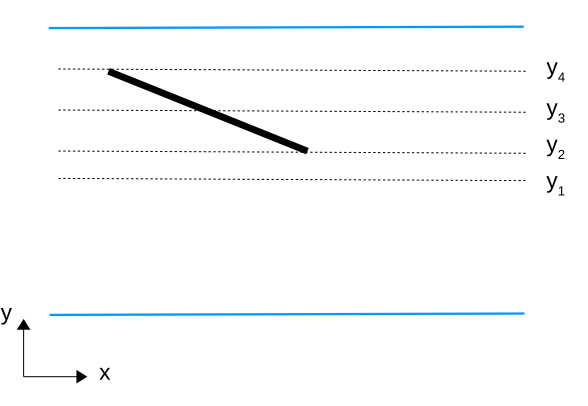


Figure 57: Planes along the span direction of the airfoil section where Cp curves are extracted..

VG simulations were carried out for the Re numbers and angle of attacks given in Table 5 for DU346 and DU396 airfoil profiles.

|     | DU     | 346    | DU396 |        |  |
|-----|--------|--------|-------|--------|--|
| Re  | 13.0e6 | 14.5e6 | 2.0e6 | 12.5e6 |  |
| AoA | -      | -      | 0.0   | 0.0    |  |
|     | -      | -      | 2.0   | 2.0    |  |
|     | 3.0    | -      | -     | -      |  |
|     | 3.5    | 3.5    | -     | -      |  |
|     | 4.0    | -      | 4.0   | 4.0    |  |
|     | -      | -      | 4.5   | 4.5    |  |
|     | 6.0    | -      | -     | -      |  |
|     | -      | 8.0    | -     | -      |  |
|     | 12.0   | 12.0   | -     | 12.0   |  |

Table 5: Simulation matrix for the VG cases.

As in the clean cases, VG case simulations were carried out until a converged solution is obtained. The simulation results are compared with the clean case results to analyze the impact of the current VG design.

15.0

15.0

In Figure 58 the lift and drag polars obtained from VG cases for 2 different Re numbers are compared with the one from the clean case for DU346 airfoil. A similar comparison

is made for DU396 airfoil for Re numbers of  $2.0\times10^6$  and  $12.5\times10^6$  (Figures 60 and 62). In all these results it can be clearly seen that introducing the VG leads to a decrease in lift coefficients and sgnificant increase in drag coefficients. This is evident in almost all the Re numbers and angle of attacks considered. The results are in contrast to the expectation of an increase in lift and a slight increase in drag coefficients due to the presence of a VG.

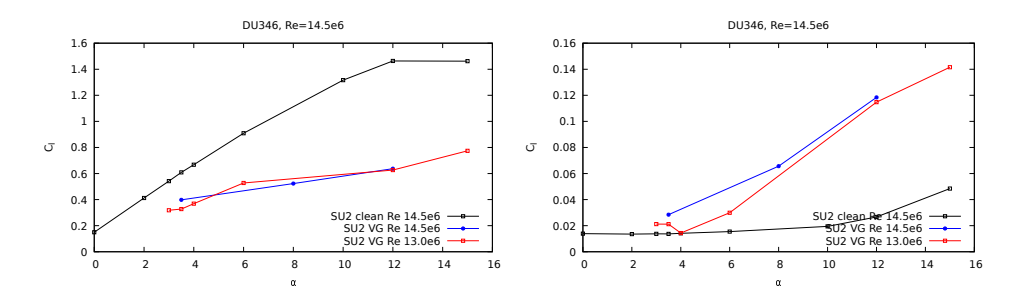


Figure 58: Lift (left) and drag (right) polar for DU346 with VG for  $Re=13.0\times10^6$  and  $Re=14.5\times10^6$  compared with the clean case for a  $Re=14.5\times10^6$ .

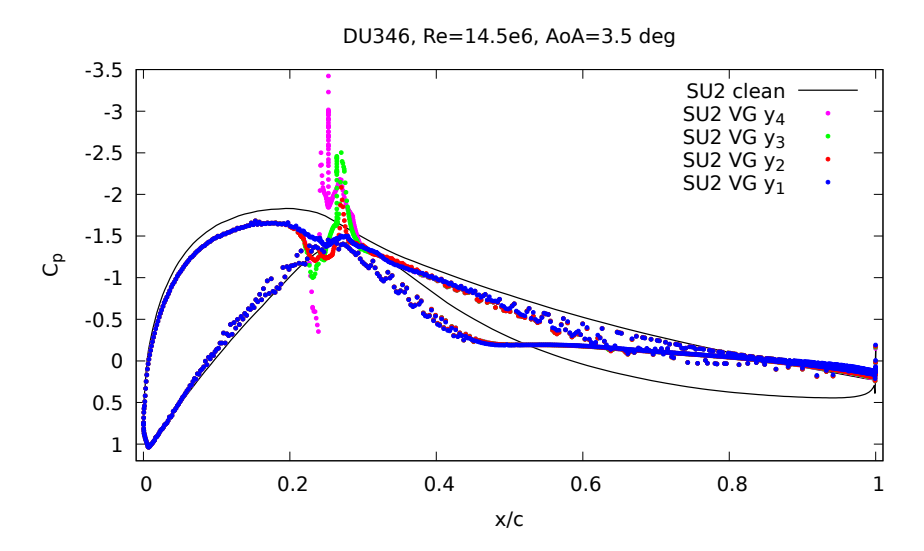


Figure 59: A comparison of pressure coefficients (Cp) for the clean and VG cases for DU346 airfoil section.  $Re=14.5\times10^6$ ,  $AoA=3.5^\circ$ .

Examining the pressure coefficient curves (Figures 59, 61 and 63) shows the effect of the VGs clearly with a peak at the location of the VGs. It is interesting to see that the highest peaks in all of these figures are at the plane passing through the leading edge of the VGs ( $y_4$ ). This result suggests a strong formation of a vortex from the leading edge of the VG. The clean Cp curves (solid black lines) from these figures show that the pressure on the pressure side at a given x-location is higher then the one on the suction side and this situation holds throughout the airfoil section for all the airfoil profiles considered. On the other hand, this statement is not true for the Cp curves for VG cases. In all three cases VGs cause a twist in the Cp curves in all x-z planes which indicates a poor performance that is in line with the results of lift and drag polars.

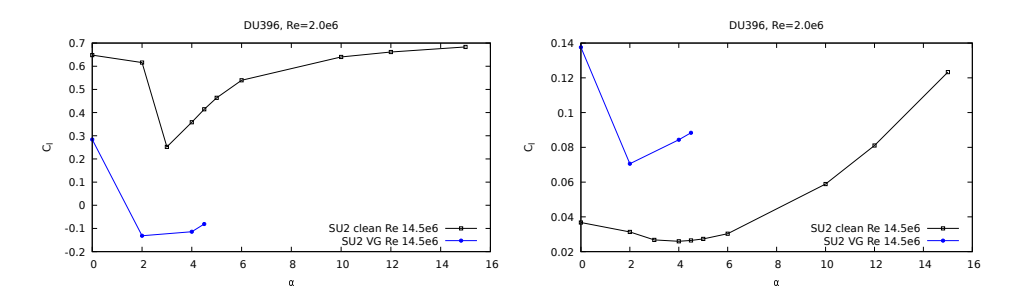


Figure 60: Lift (left) and drag (right) polar for DU396 with VG for  $Re=2.0\times10^6$  compared with the clean case.

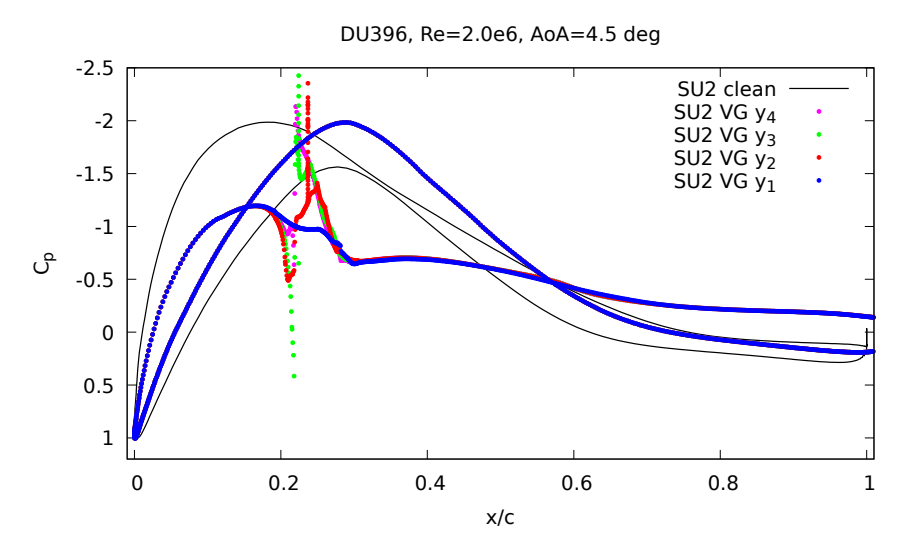


Figure 61: A comparison of pressure coefficients (Cp) for the clean and VG cases for DU396 airfoil section.  $Re=2.0\times10^6,\,AoA=4.5^\circ$  .

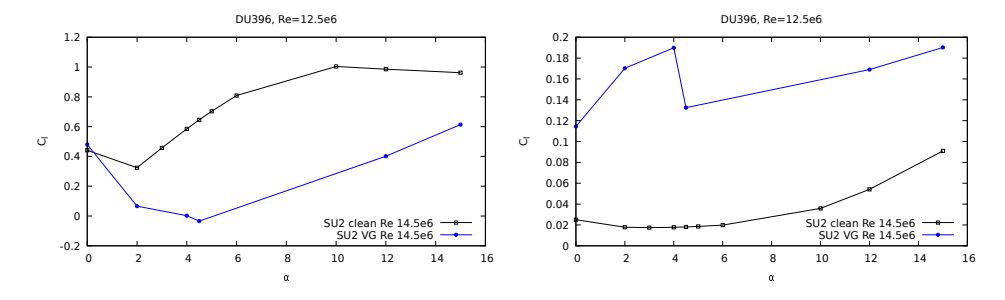


Figure 62: Lift (left) and drag (right) polar for DU396 with VG for  $Re=12.5\times10^6$  compared with the clean case.

In order to understand this poor performance of VG these cases were analyzed further. In a conventional VG design, the height of the VG is slightly larger than the height of the boundary layer where the tip of the VG is closer to the edge of the boundary layer. Thus, mildly separated flow can mix with the boundary layer and energize it which leads to the flow remaining attached for longer. Consequently, the stall is delayed. In the current design case however, as seen in Figure 64, the separation at the top of the VG is quite considerable due to the size of the VG and the distance of the tip of the VG is quite far away from the edge of the boundary layer which prevents

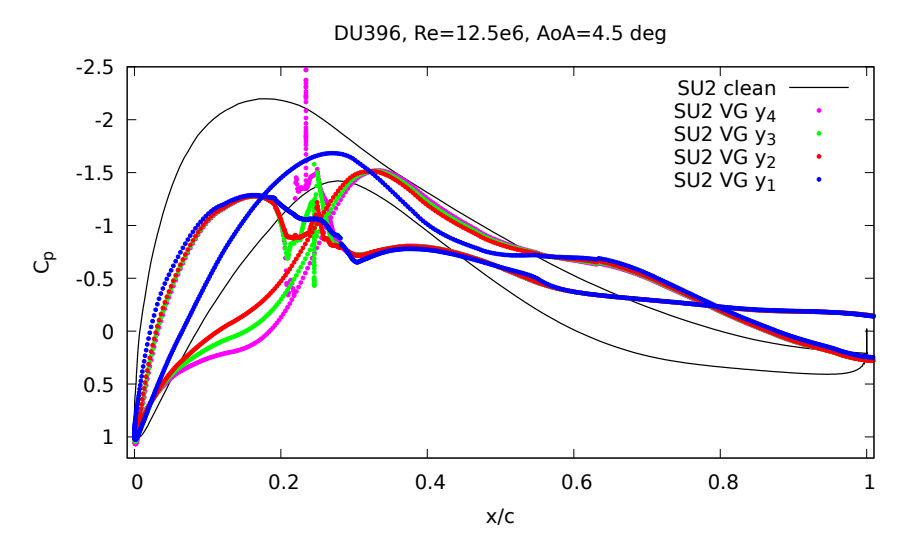


Figure 63: A comparison of pressure coefficients (Cp) for the clean and VG cases for DU396 airfoil section.  $Re=12.5\times10^6,\,AoA=4.5^\circ$  .

the mixing of this outer flow with the boundary layer. In the current design the height of the VG is several times larger then the boundary layer thickness.

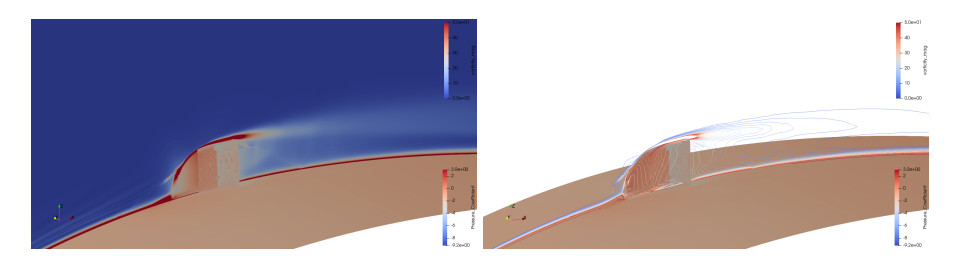


Figure 64: Vorticity magnitude for DU346  $Re=12.5\times10^6$ ,  $AoA=2.0^\circ$  (left) with contours (right).

In Figure 65 the vorticity magnitude in the two planes downstream of the VG is presented. Closer look at this picture shows two high vorticity regions one being around the airfoil surface which also marks the boundary layer height (approximately) and the other region just downstream of the tip of the VG indicating the shed vortex from the VG. It is also clearly evident from this figure that this shed vortex is too far away from the boundary layer and does not mix. Instead it is convected downstream as seen from Figure 66.

In Figure 67 a simulation detail from a conventional VG design is presented where the mixing of the shed vortices with the boundary layer region can be clearly seen.

In Figure 68 velocity profiles before and after the VGs for the current (left) and for a conventional design (right) is shown (please note the scale difference in y-axis). The current design is for an airfoil section with a chord length of 6.0m and the conventional design is for an airfoil section with a chord length of 1.0m. Considering the velocity profile just before the VG location (x = 1.253) for the current design, the height of the boundary layer can be determined approximately around 0.02 - 0.03m. The effect of the VG on the velocity profile can be seen at the station x = 1.327 where velocity has

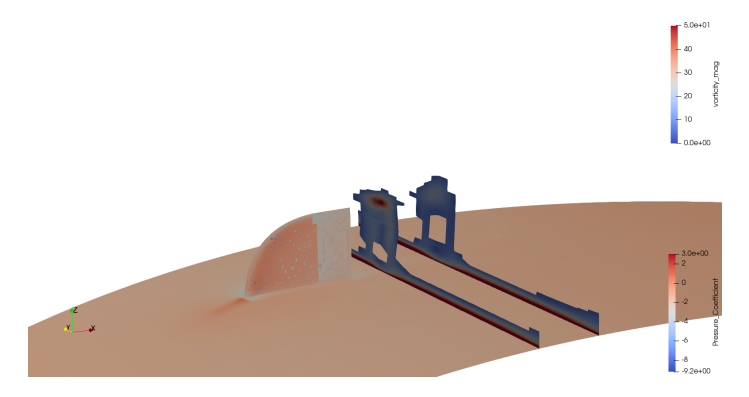


Figure 65: Vorticity on the planes behind the VG for DU346  $Re=12.5\times10^6$ ,  $AoA=2.0^\circ$ .

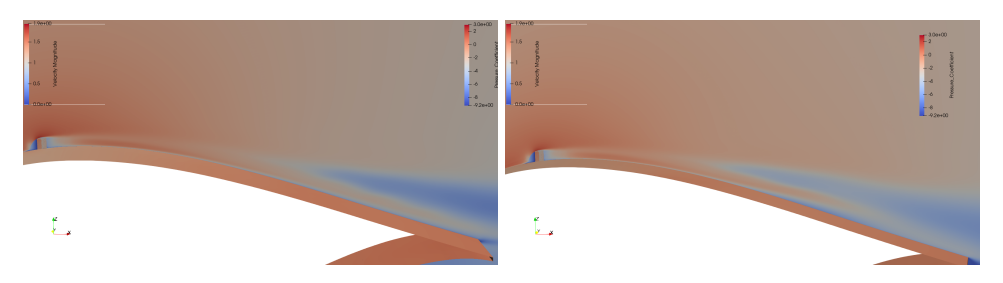


Figure 66: Velocity behind the VG for DU346  $Re=12.5\times10^6,\ AoA=2.0^\circ$  (left)  $AoA=12.0^\circ$  (right).

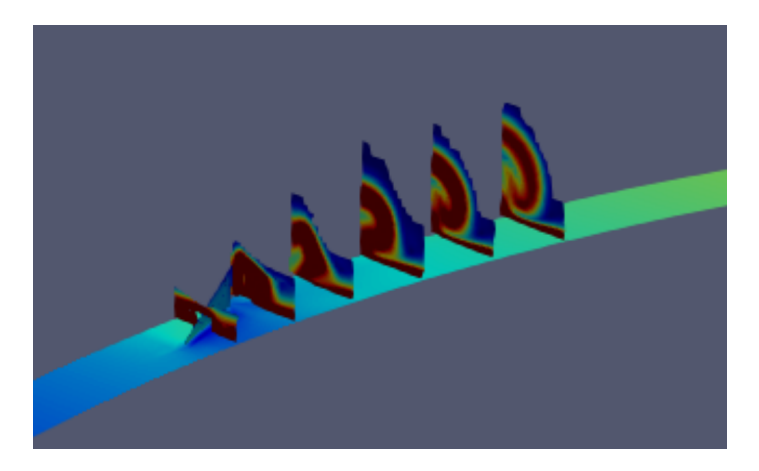
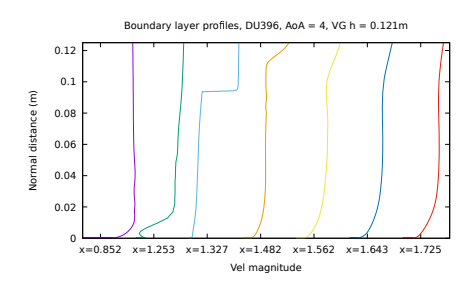


Figure 67: Vorticity behind the VG for FFA241  $Re=1.6\times10^6$ ,  $AoA=8.8^\circ$  (an example simulation with a conventional VG design).

a sudden increase around y=0.1m which corresponds to the height of the VG. After this point, the deflection in the velocity profile due to VG travels below the tip of the VG but it doesn't reach as far as the boundary layer edge.

This situation is evident from the last velocity layer profile at x=1.725 where the velocity stays almost constant between the edge of the boundary layer (around y=0.03m) until around y=0.1m. When the conventional case is considered (right of Figure 68) this mixing can be clearly seen, e.g. by looking at the last velocity profile at x=0.187 where it starts deflecting right after the edge of the boundary layer suggesting a boundary layer mixing due to the VG.



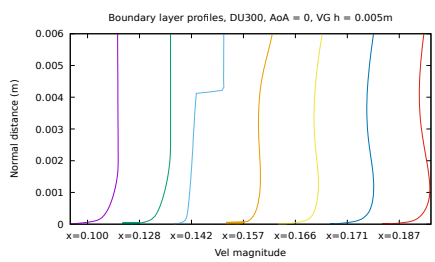


Figure 68: Boundary layer profiles on the airfoil near the VG for DU 396 with S2V1 with h=0.121m for an airfoil section with a chord length of 6.0m (left) and for a conventional VG with h=0.005m for an airfoil section with a chord length of 1.0m (right).

From the simulation results presented in this section it can be concluded that the first iteration of the VG design performs under the expectations. From this point on the rest of the tasks to quantify the effect of VGs on the performance of the blade was not continued.

#### 6 Conclusions

This project aims for the design and development of an innovative solution for wind turbine blade leading edge protection, namely "fit-for-purpose sleeve", which couples the leading edge protection with vortex generators (VGs) and the development of the requisite numerical tools to analyze such innovative wind energy applications. To this end a sleeve design was made and the necessary numerical tools required for analysis of such configurations was developed.

One of the main tasks of this project is to develop a pressure-based incompressible Navier-Stokes method and implement it in the open source CFD suite SU2 and apply it for the above mentioned VG design to analyze the effect on the performance on a blade. As the first main deliverable the development of the CFD method is completed and the method together with verification and validation is published and presented on various platforms including the AIAA SciTech 2020 Conference and SU2 developers meeting. The (extended) details of the method and the verification and validation cases are also presented in this report. It is shown that the developed method is capable of simulating VGs with body fitted meshes. Additionally, a model to analyze leading edge roughness is also implemented in the open source suite.

In the second part of the project the main goal was to apply the new pressure-based method to simulate airfoil sections with and without VGs. For this purpose the generic AVATAR blade is chosen as the base blade and Laminar Flow Technology Limited (LFTL) has performed the VG design.

First of all, the CFD simulations were carried out on the five "clean" airfoil sections (without VGs) of the AVATAR blade and lift and drag polars as well as pressure coefficient distributions are obtained. It is shown that these CFD simulation results are in good agreement with the numerical results obtained by the in-house aerodynamic design and analysis tool RFOIL.

After the final VG configuration details received from LFTL, body fitted VG meshes were generated for DU346, DU396 and DU600 sections of the AVATAR blade. Initially, the simulations were performed for DU346 and DU396 airfoil sections for various Re numbers and angle of attacks. The analysis of these simulations revealed that the performance of the VGs did not match the expectations e.g. they decreased the lift and increased the drag considerably while an increase in lift and a slight increase in drag coefficients were expected. This is a significant result of the study that has been performed in collaboration with LFTL.

In a conventional design, the height of the VG is slightly larger than the height of the boundary layer where the tip of the VG is closer to the edge of the boundary layer. Thus, mildly separated flow can mix with the boundary layer and energize it. Further analysis of the current VGs revealed that the sizes (heights) of the VGs were considerably larger then the heights of the boundary layer and the mixing of the

boundary layer with the outer flow does not occur. Also, due to the height of the VG, the flow lifts away from the airfoil surface and separates earlier. These unexpected effects could also be seen from the lift and drag polars as well as from the pressure coefficient graphs.

Because of the disappointing results for the airfoils, it is not expected that a blade design using these vortex generators will improve performance. For that reason, the performance analysis of the blade with and without VGs was not completed. This project achieved the following milestones:

- Development of a pressure-based incompressible Navier-Stokes method for wind energy applications.
- · Mesh generation for complex geometries.
- Capability of simulating critical wind energy applications like VGs and leading edge roughness.
- · Experience in the vortex generator design methodology.
- First steps towards establishing an automated framework to extract various boundary layer parameters from CFD solutions which can be used to enhance RFOIL further.

A natural follow-up of this project would be making a new VG design with the help of the analysis already performed and complete the performance analysis as intended. Furthermore, in a new project the effect of the leading edge roughness on the performance of a blade can also be analyzed in details.

#### 7 References

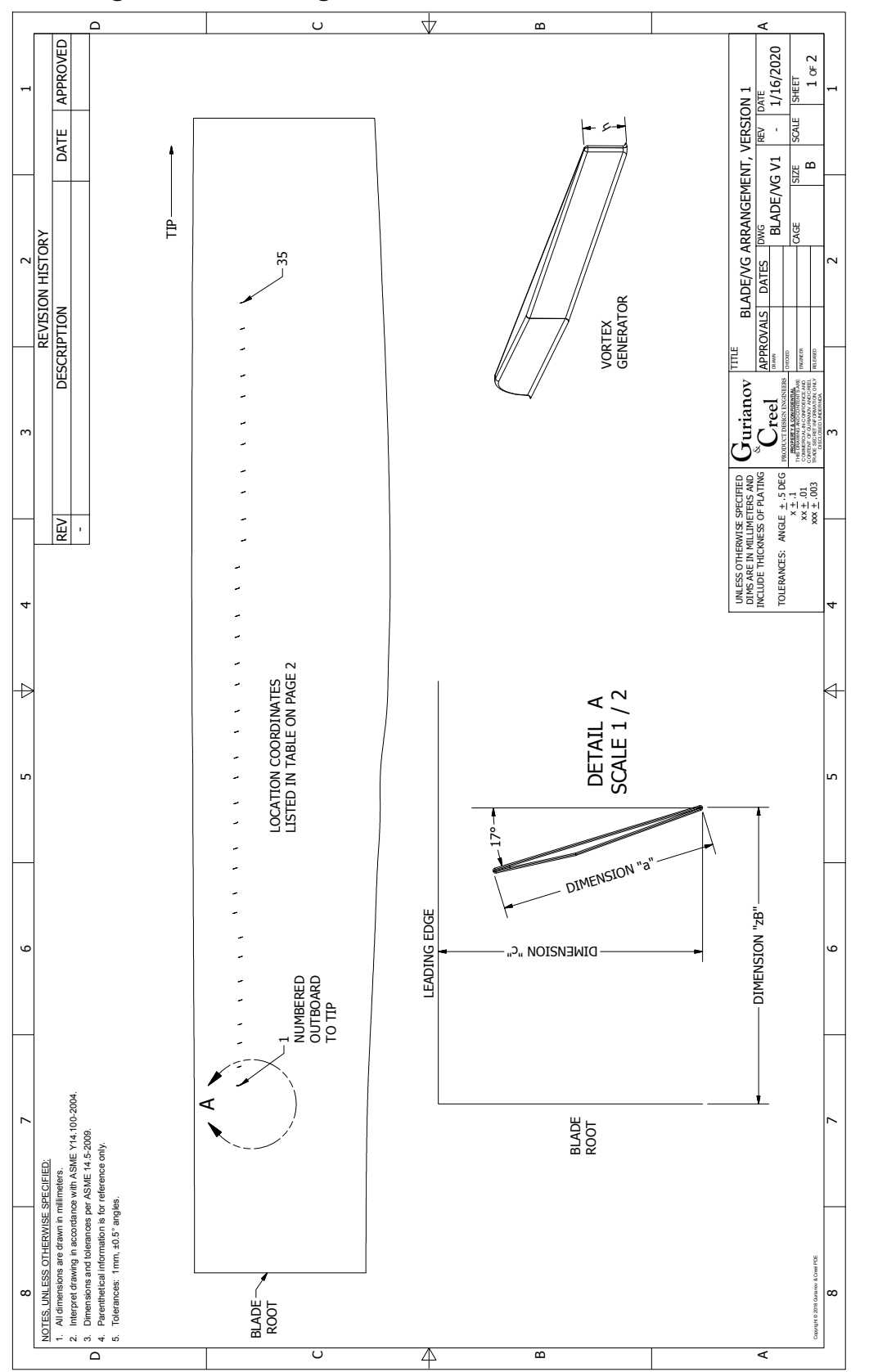
- [1] U. Ghia, K. N. Ghia, and C. T. Shin. High-Re solutions for incompressible flow using Navier-Stokes equations and a multigrid method. *Journal of Computational Physics*, 48(3):387–411, 1982.
- [2] A. K. Ravishankara, H. Özdemir, and E.T.A. van der Weide. Implementation of a pressure based incompressible flow solver in su2 for wind turbine applications. In *AIAA SciTech 2020 Forum*, number AIAA-2020-0992.
- [3] J. Manwell, J. Mcgowan, and A. L. Rogers. *Wind Energy Explained: Theory, Design and Application, Second Edition*, volume 30. 03 2006.
- [4] J.G. Schepers. Engineering models in wind energy aerodynamics: Development, implementation and analysis using dedicated aerodynamic measurements. PhD thesis, Delft University of Technology, 2012.
- [5] J. Katz and A. Plotkin. *Low-Speed Aerodynamics*. Cambridge Aerospace Series. Cambridge University Press, 2nd edition, 2001.
- [6] M. Drela. Xfoil: An analysis and design system for low reynolds number airfoils. In *Low Reynolds number aerodynamics*, pages 1–12. Springer, 1989.
- [7] R. P. J. O. M. Rooij van. Modification of the boundary layer in RFOIL for improved stall prediction. Report IW-96087R, Delft University of Technology, Delft, The Netherlands, September 1996.
- [8] G. Ramanujam, H. Özdemir, and H. W. M. Hoeijmakers. Improving airfoil drag prediction. *Journal of Aircraft*, 53(6):1844–1852, 2016.
- [9] G. Ramanujam and H. Özdemir. Improving airfoil lift prediction. In *AIAA SciTech* 35th Wind Energy Symposium, number AIAA-2017-1999, 2017.
- [10] R. Vaithiyanathasamy, H. Özdemir, G. Bedon, and A. Garrel van. A double wake model for interacting boundary layer methods. In AIAA SciTech 2018 Forum, pages AIAA–2018–0516, 2018.
- [11] H. G. Weller, G. Tabor, H. Jasak, and C. Fureby. A tensorial approach to computational continuum mechanics using object-oriented techniques. *Computers in Physics*, 12(6):620–631, 1998.
- [12] J. A. Michelsen. Basis3d a platform for development of multiblock pde solvers. Technical Report AFM 92-05, Technical University of Denmark, 1992.
- [13] J. A. Michelsen. Block structured multigrid solution of 2d and 3d elliptic pde's. Technical Report AFM 94-06, Technical University of Denmark, 1994.
- [14] F. Palacios, M. R. Colonno, A. Aranake, A. Campos, S. R. Copeland, T. D. Economon, A. Lonkar, T. W. Lukaczyk, T. W. R. Taylor, and J. J. Alonso. Stanford University Unstructured (SU2): An open-source integrated computational environment for multi-physics simulation and design. 2013.

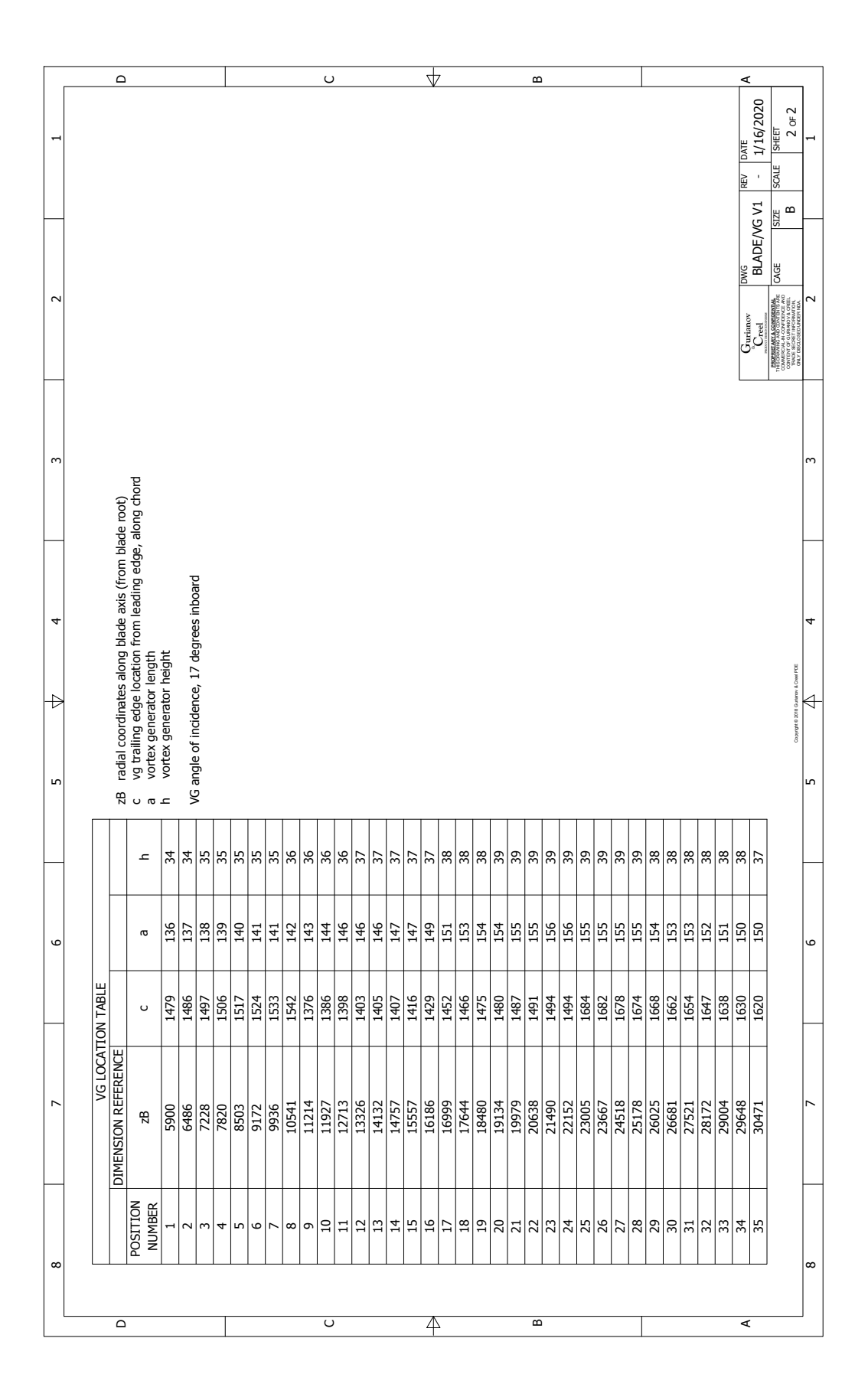
- [15] F. Palacios, S. Padron, B. Tracey, D. E. Manosalvas, A. Aranake, S. R. Copeland, A. Variyar, J. J. Alonso, T. W. Lukaczyk, A. K. Lonkar, K. R. Naik, and T. D. Economon. Stanford University Unstructured (SU2): Analysis and Design Technology for Turbulent Flows. (January):1–33, 2014.
- [16] F. Porté-Agel, M. Bastankhah, and S. Shamsoddin. Wind-turbine and wind-farm flows: A review. *Boundary-Layer Meteorology*, Sep 2019.
- [17] P. Spalart and S. Allmaras. A one-equation turbulence model for aerodynamic flows. In 30th aerospace sciences meeting and exhibit, page 439, 1992.
- [18] F. R. Menter. Two-equation eddy-viscosity turbulence models for engineering applications. AIAA Journal, 32(8):1598–1605, 1994.
- [19] S. C. Cakmakcioglu, Bas. O., and U. Kaynak. A correlation-based algebraic transition model. *Proceedings of the Institution of Mechanical Engineers, Part* C: Journal of Mechanical Engineering Science, 232(21):3915–3929, 2018.
- [20] F. R. Menter, R. Langtry, and S. Völker. Transition modelling for general purpose cfd codes. *Flow, Turbulence and Combustion*, 77(1):277–303, Nov 2006.
- [21] D. Kwak and C. Kiris. Success and Challenges in Incompressible Flow Simulation. AIAA, 2003.
- [22] D. Kwak, C. Kiris, and C. S. Kim. Computational challenges of viscous incompressible flows. *Computers and Fluids*, 34(3):283 299, 2005.
- [23] J. H. Ferziger, M. Perić, and M. Peric. *Computational Methods for Fluid Dynamics*. Springer, third edition, 2002.
- [24] F. Moukalled, L. Mangani, and M. Darwish. Fluid Mechanics and Its Applications The Finite Volume Method in Computational Fluid Dynamics An Advanced Introduction with OpenFOAM® and Matlab®. Springer, 2015.
- [25] Wei Shyy. Elements of Pressure-Based Computational Algorithms. Advances in Heat Transfer, 24(C):191–275, 1994.
- [26] C. Hirsch. Numerical computation of internal and external flows. Wiley, 1997.
- [27] C. A. Park and D. Kwak. On the Method of Pseudo Compressibility for Numerically Solving Incompressible Flows. In 22nd Aerospace Sciences Meeting. AIAA, 1984.
- [28] A. J. Chorin. A numerical method for solving incompressible viscous flow problems. *Journal of computational physics*, 2(1):12–26, 1967.
- [29] T. D. Economon. Simulation and adjoint-based design for variable density incompressible flows with heat transfer. *AIAA Journal*, pages 1–13, 2019.
- [30] F.H. Harlow and J.E. Welch. Numerical Calculation of Time-Dependent Viscous Incompressible Flow with Free Surface. *Physics of FLuids*, 8(12), 1965.
- [31] S. V. Patankar and D. B. Spalding. A calculation procedure for heat, mass and momentum transfer in three-dimensional parabolic flows. *International Journal* of Heat and Mass Transfer, 1972.

- [32] S. V. Patankar. Numerical heat transfer and fluid flow. CRC press, 1980.
- [33] C M Rhie and W L Chowt. Numerical Study of the Turbulent Flow Past an Airfoil with Trailing Edge Separation. *AIAA Journal*, 21(11), 1983.
- [34] S. Majumdar. Role of underrelaxation in momentum interpolation for calculation of flow with nonstaggered grids. *Numerical Heat Transfer*, 13(1):125–132, 1988.
- [35] S. K. Choi. Note on the use of momentum interpolation method for unsteady flows. *Numerical Heat Transfer Part a-Applications*, 36(August 1998):545–550, 1999.
- [36] W. Z. Shen, J. A. Michelsen, and J. N. Sorensen. Improved Rhie-Chow interpolation for unsteady flow computations. AIAA Journal, 39(12):2406–2409, 2012.
- [37] A. Cubero and N. Fueyo. A compact momentum interpolation procedure for unsteady flows and relaxation. *Numerical Heat Transfer, Part B: Fundamentals*, 52(6):471–493, 2007.
- [38] P. Bartholomew, F. Denner, M. H. Abdol-Azis, A. Marquis, and B. G.M. Wachem van. Unified formulation of the momentum-weighted interpolation for collocated variable arrangements. *Journal of Computational Physics*, 375:177–208, 2018.
- [39] J. Blazek. Unstructured finite volume schemes. In J. Blazek, editor, Computational Fluid Dynamics: Principles and Applications (Second Edition), pages 131 182. Elsevier Science, Oxford, second edition edition, 2005.
- [40] T. J. Barth. Aspects of unstructured grids and finite-volume solvers for the euler and navier-stokes equations. Technical Report NASA-92N27677, 1992.
- [41] B. Yu, Y. Kawaguchi, W. Q. Tao, and H. Ozoe. Checkerboard pressure predictions due to the underrelaxation factor and time step size for a nonstaggered grid with momentum interpolation method. *Numerical Heat Transfer, Part B: Fundamentals*, 41(1):85–94, 2002.
- [42] J. Y. Murthy and S. Mathur. Periodic flow and heat transfer using unstructured meshes. *International Journal for Numerical Methods in Fluids*, 25(6):659–677, 2002.
- [43] H. Xiao, J. Wang, Z. Liu, and W. Liu. A consistent SIMPLE algorithm with extra explicit prediction SIMPLEPC. *International Journal of Heat and Mass Transfer*, 120:1255–1265, 2018.
- [44] Y. Ruey-Hor and L. Chen-Hua. Enhancement of the simple algorithm by an additional explicit corrector step. *Numerical Heat Transfer, Part B: Fundamentals*, 24(1):127–141, 1993.
- [45] I. Sezai. Implementation of boundary conditions in pressure-based finite volume methods on unstructured grids. *Numerical Heat Transfer, Part B: Fundamentals*, 72(1):82–107, 2017.
- [46] M. Darwish, L. Mangani, and F. Moukalled. Implicit boundary conditions for coupled solvers. *Computers and Fluids*, 168(2018):54–66, 2018.

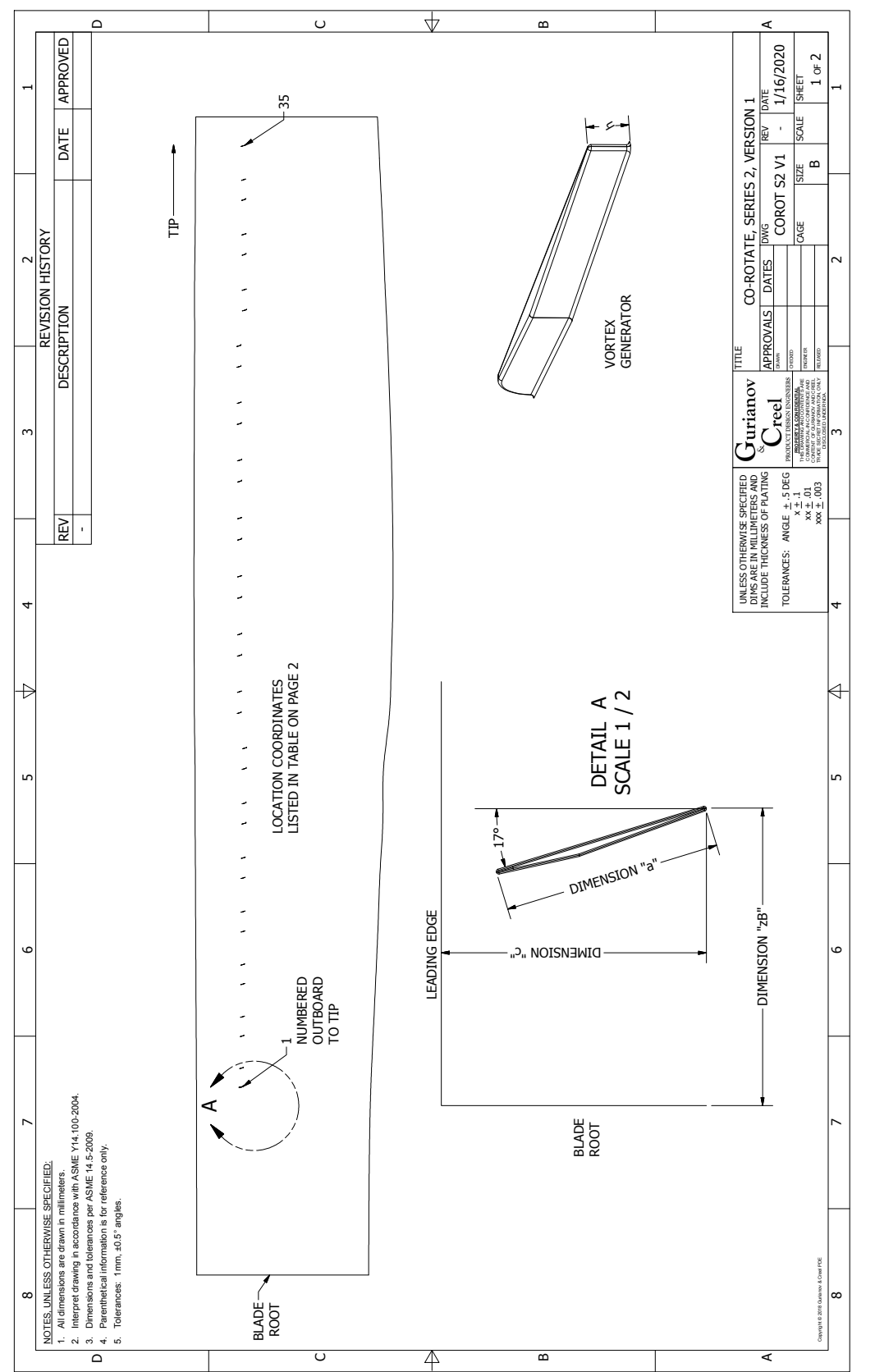
- [47] H.M. Lyon. Boundary Layer Theory, volume 7. 2014.
- [48] R. Gautier, D. Biau, and E. Lamballais. A reference solution of the flow over a circular cylinder at re=40. *Computers & Fluids*, 75:103 111, 2013.
- [49] D. K. Gartling. A test problem for outflow boundary conditions—flow over a backward-facing step. *International Journal for Numerical Methods in Fluids*, 11(7):953–967, 1990.
- [50] C. Rumsey. Nasa turbulence modeling resource. https://turbmodels.larc. nasa.gov/index.html, 2019.
- [51] C. L. Ladson. Effects of independent variation of mach and reynolds numbers on the low-speed aerodynamic characteristics of the naca 0012 airfoil section. Technical Report NASA-TM-4074, NASA, 1988.
- [52] J.G. Schepers, K. Boorsma, N. Sørensen, S. G. Voutsinas, H. Rahimi, H. Heisselmann, E. Jost, T. Lutz, T. Maeder, A. Gonzalez, C. Ferreira, B. Stoevesandt, G. Barakos, N. Lampropoulos, A. Croce, and J. Madsen. Final results from the EU project AVATAR: Aerodynamic modelling of 10 MW wind turbines. *Journal of Physics: Conference Series*, 1037:022013, jun 2018.
- [53] D. Baldacchino, C. S. Ferreira, D. Tavernier De, W. A. Timmer, and G. J. W. Bussel van. Experimental parameter study for passive vortex generators on a 30% thick airfoil. *Wind Energy*, 21(9):745–765, 2018.
- [54] A. K. Ravishankara, I. Bakhmet, and H. Özdemir. Estimation of roughness effects on wind turbine blades with vortex generators. In *The Science of Making Torque from Wind (TORQUE 2020), accepted for publication.*

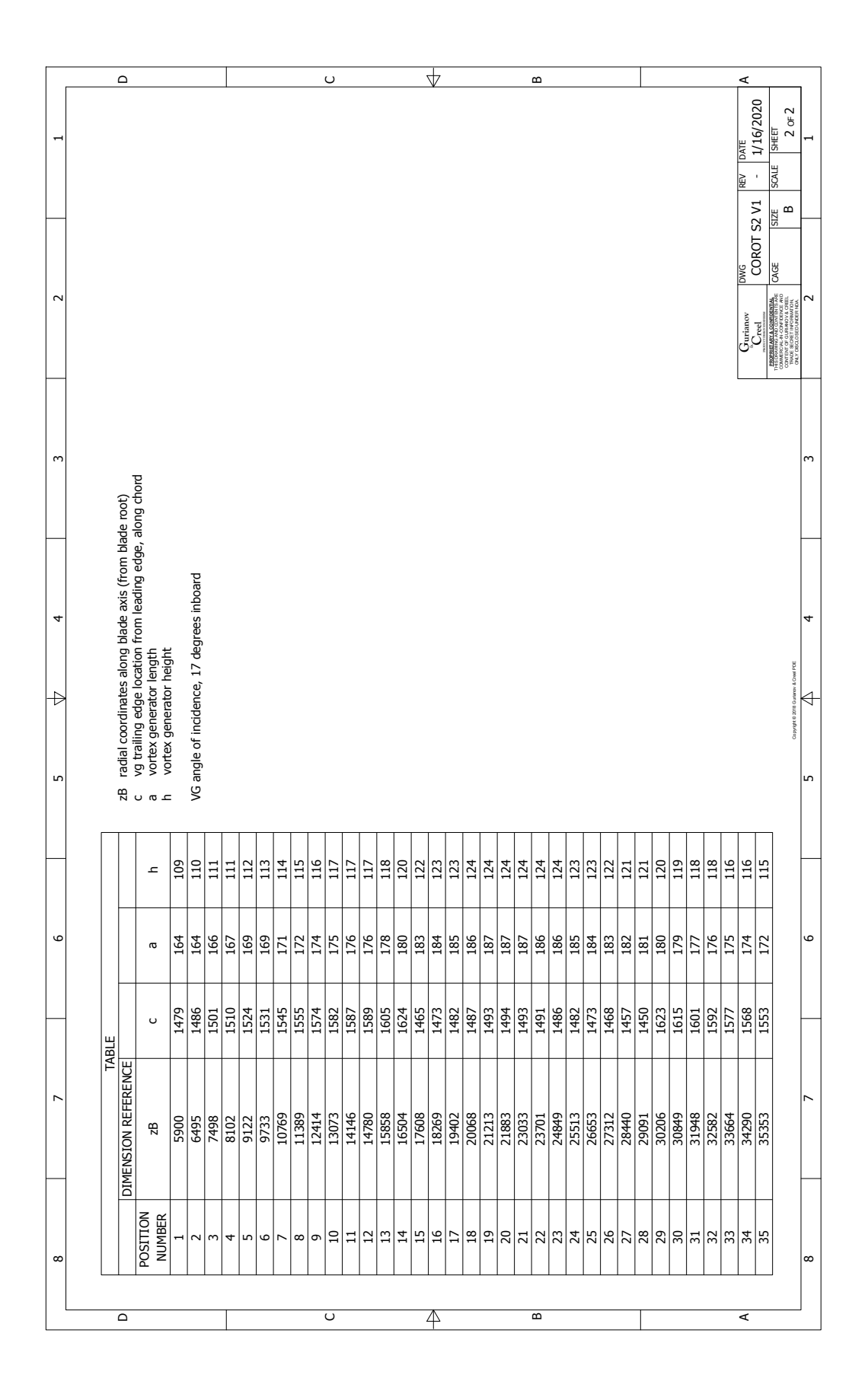
## A VG design: co-rotating series 1 version 1



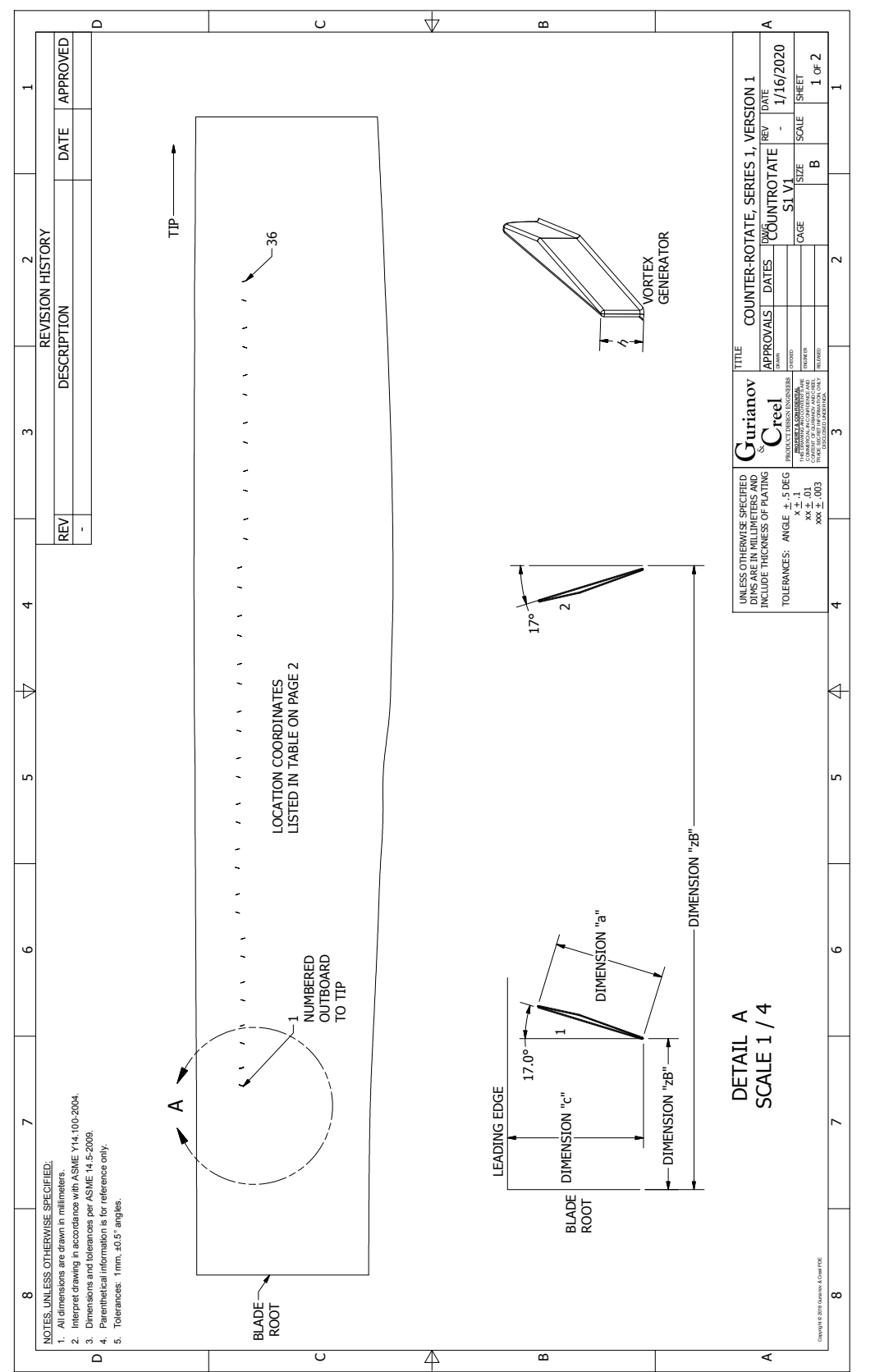


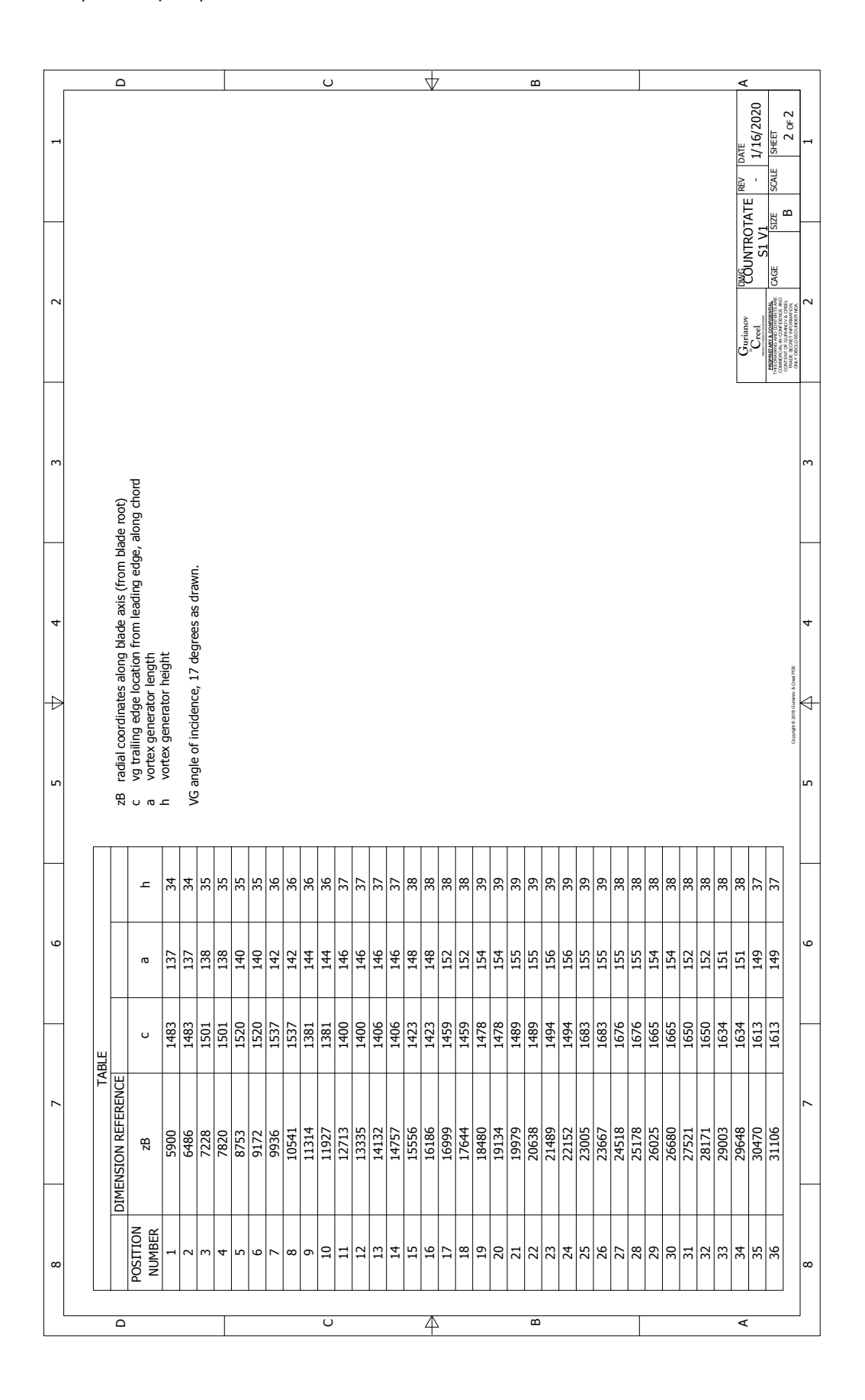
## B VG design: co-rotating series 2 version 1



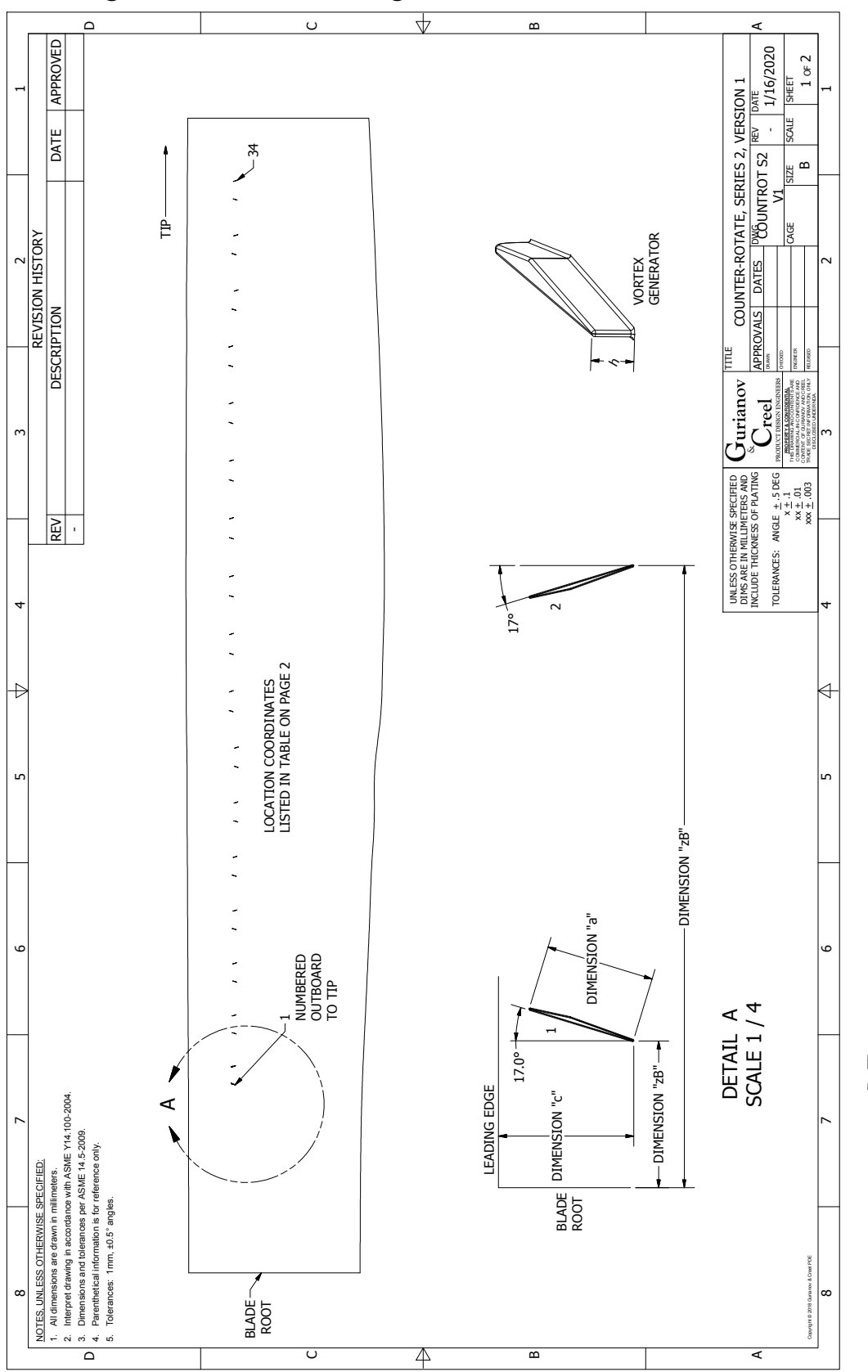


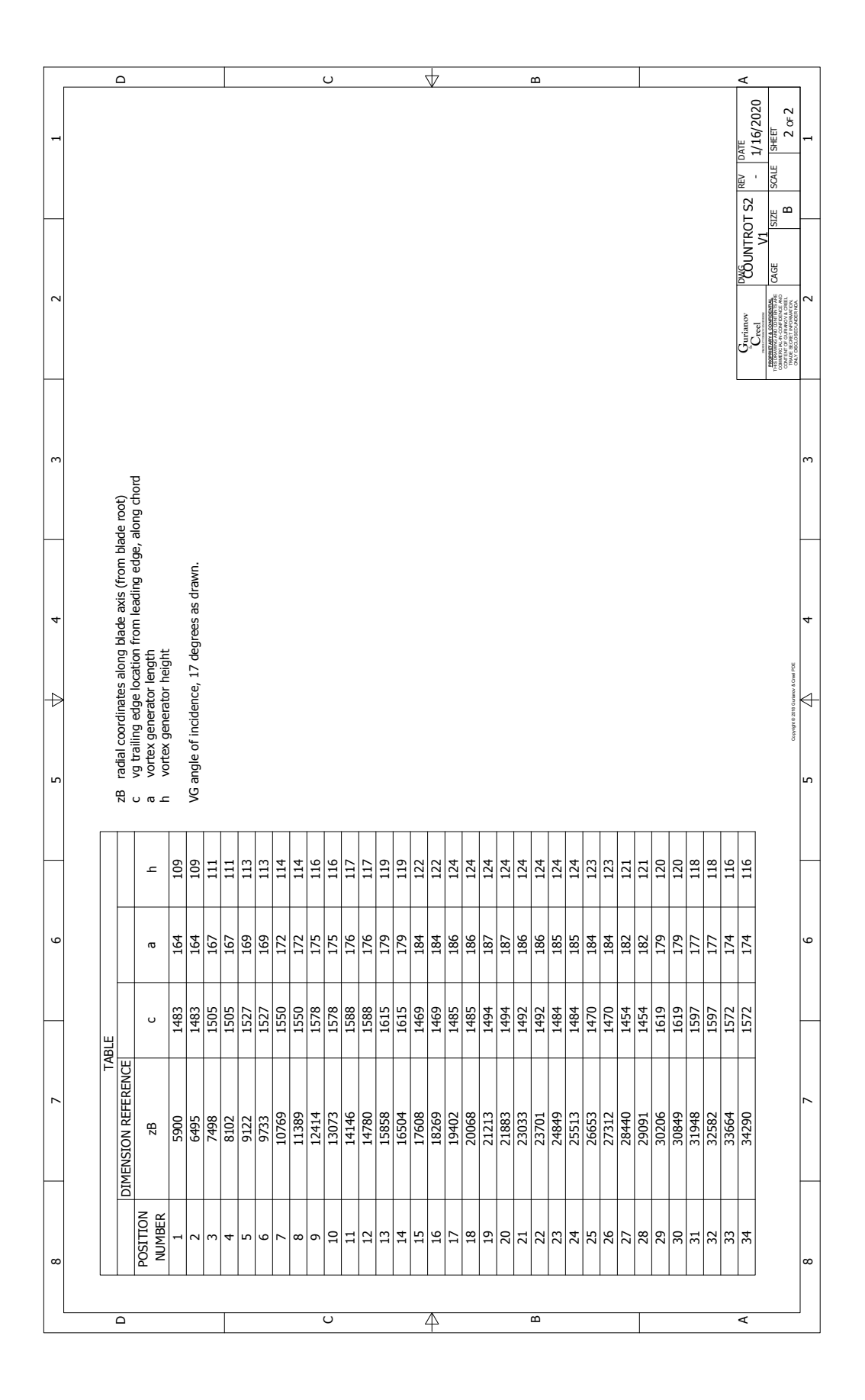
## C VG design: counter-rotating series 1 version 1



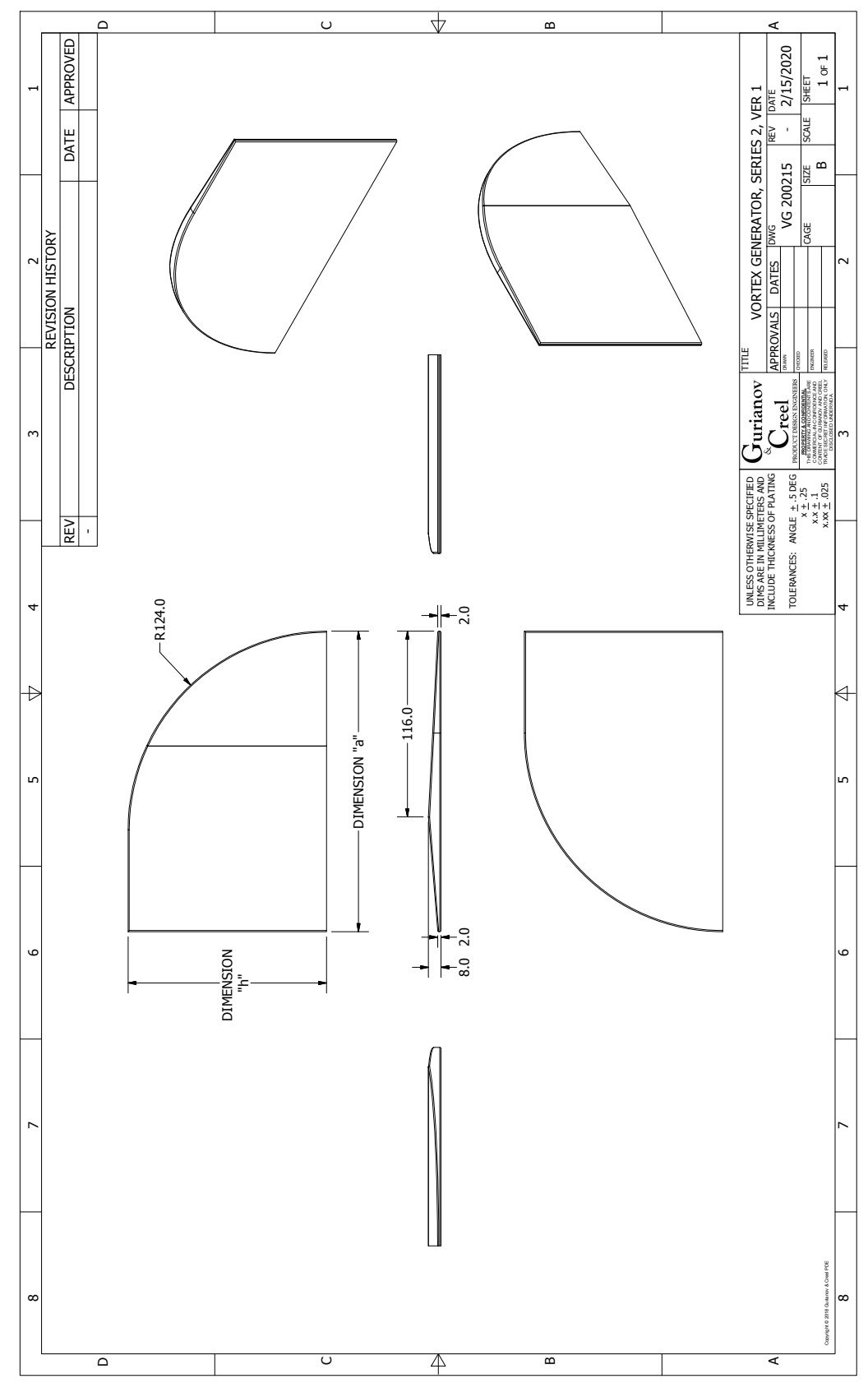


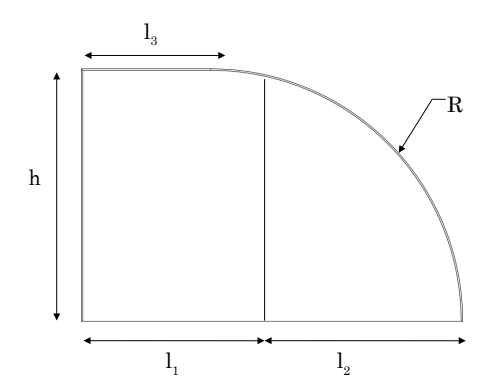
## D VG design: counter-rotating series 2 version 1





# E VG design: counter-rotating series 2 version 1 - final dimensions





- Each of these dimensions needed at every zB location along the span of the blade.
- At each zB location the distance of the VG from the leading edge of the blade is also needed.

ALL DIMENSIONS IN MILLIMETERS

| Position | zB    | Dist.from<br>leading<br>edge | h   | R   | L3 | L2 | L1  |
|----------|-------|------------------------------|-----|-----|----|----|-----|
| 1        | 5900  | 1319                         | 109 | 109 | 55 | 63 | 101 |
| 2        | 6495  | 1319                         | 109 | 109 | 55 | 63 | 101 |
| 3        | 7498  | 1338                         | 111 | 111 | 56 | 64 | 103 |
| 4        | 8102  | 1338                         | 111 | 111 | 56 | 64 | 103 |
| 5        | 9122  | 1358                         | 113 | 113 | 56 | 65 | 104 |
| 6        | 9733  | 1358                         | 113 | 113 | 56 | 65 | 104 |
| 7        | 10769 | 1378                         | 114 | 114 | 58 | 66 | 106 |
| 8        | 11389 | 1378                         | 114 | 114 | 58 | 66 | 106 |
| 9        | 12414 | 1403                         | 116 | 116 | 59 | 67 | 108 |
| 10       | 13073 | 1403                         | 116 | 116 | 59 | 67 | 108 |
| 11       | 14146 | 1412                         | 117 | 117 | 59 | 67 | 109 |
| 12       | 14780 | 1412                         | 117 | 117 | 59 | 67 | 109 |
| 13       | 15858 | 1436                         | 119 | 119 | 60 | 68 | 111 |
| 14       | 16504 | 1436                         | 119 | 119 | 60 | 68 | 111 |
| 15       | 17608 | 1285                         | 122 | 122 | 62 | 70 | 114 |
| 16       | 18269 | 1285                         | 122 | 122 | 62 | 70 | 114 |
| 17       | 19402 | 1299                         | 124 | 124 | 62 | 71 | 115 |
| 18       | 20068 | 1299                         | 124 | 124 | 62 | 71 | 115 |
| 19       | 21213 | 1307                         | 124 | 124 | 63 | 71 | 116 |
| 20       | 21883 | 1307                         | 124 | 124 | 63 | 71 | 116 |
| 21       | 23033 | 1306                         | 124 | 124 | 62 | 71 | 115 |
| 22       | 23701 | 1306                         | 124 | 124 | 62 | 71 | 115 |
| 23       | 24849 | 1299                         | 124 | 124 | 61 | 71 | 114 |

| 24 | 25513 | 1299 | 124 | 124 | 61 | 71 | 114 |
|----|-------|------|-----|-----|----|----|-----|
| 25 | 26653 | 1286 | 123 | 123 | 61 | 70 | 114 |
| 26 | 27312 | 1286 | 123 | 123 | 61 | 70 | 114 |
| 27 | 28440 | 1272 | 121 | 121 | 61 | 70 | 112 |
| 28 | 29091 | 1272 | 121 | 121 | 61 | 70 | 112 |
| 29 | 30206 | 1440 | 120 | 120 | 59 | 68 | 111 |
| 30 | 30849 | 1440 | 120 | 120 | 59 | 68 | 111 |
| 31 | 31948 | 1420 | 118 | 118 | 59 | 68 | 109 |
| 32 | 32582 | 1420 | 118 | 118 | 59 | 68 | 109 |
| 33 | 33664 | 1398 | 116 | 116 | 58 | 66 | 108 |
| 34 | 34290 | 1398 | 116 | 116 | 58 | 66 | 108 |